A CHARACTERISTIC MODE ANALYSIS OF CONDUCTIVE NANOWIRES AND MICROWIRES ABOVE A LOSSY DIELECTRIC HALF-SPACE

A THESIS IN

Electrical Engineering

Presented to the Faculty of the University
of Missouri-Kansas City in partial fulfillment of
the requirements for the degree

MASTER OF SCIENCE

by
DANIEL S. KIDDLE

B.E., Electrical and Computer Engineering,
University of Kansas City-Missouri, Kansas City, Missouri, 2016

Kansas City, Missouri

2017

A CHARACTERISTIC MODE ANALYSIS OF CONDUCTIVE NANOWIRES AND MICROWIRES ABOVE A LOSSY DIELECTRIC HALF-SPACE

Daniel S. Kiddle, Candidate for the Master of Science Degree

University of Missouri – Kansas City, 2017

ABSTRACT

Nanowires possess extraordinary mechanical, thermoelectric and electromagnetic properties which led to their incorporation in a wide variety of applications. The purpose of this study is to investigate the effect of material on the electromagnetic response of these nanowires. We used the Method of Moments (MOM) for Arbitrarily Thin Wire (ATW) formulation as an efficient computational technique for calculating the electromagnetic response of nanowires. To explain the calculated electromagnetic response, we evoked the Characteristic Mode Analysis (CMA) which decomposes the current on the wire into a superposition of fundamental current modes. These modes are weighted by two coefficients: (*i*) the relative importance of each mode at a certain frequency, termed Modal Significance, and (*ii*) the level of coupling between the incident field and the mode termed the Modal Excitation Coefficient. In this, work we study how the wire's material affect the Modal Significance and the Modal Excitation Coefficient of nanowires. Our results show that the

material of the nanowire has a strong effect on the resonance frequency, the bandwidth, and the overlap of the modes showing that the material of the nanowire can be used as a tuning factor to develop sensors with desired radiation characteristics.

Nanowires are commonly grown vertically on a substrate and, therefore, we also study the effect of the presence of a lossy dielectric half-space on their electromagnetic response. To efficiently account for this interface, we utilize a modified Green's function using the rigorous Sommerfeld integrals. Our results show that the relative permittivity of the substrate decreases the resonance frequencies of the nanowires and significantly alters their radiation patterns. Most importantly, we find that, if the nanowire is near the interface, its evanescent field's couple to the dielectric half space leading to the majority of the scattered power radiated into the substrate with high directivity. The results of this thesis has the potential to quantify the electromagnetic response of vertical nanowires in their realistic environment as well as facilitate the incorporation of nanowires in novel sensing applications.

APPROVAL PAGE

The faculty listed below, appointed by the Dean of the School of Computing and Engineering, have examined a thesis titled "A Characteristic Mode Analysis of Conductive Nanowires and Microwires Above a Lossy Dielectric Half-Space" presented by Daniel Kiddle, candidate for the Master of Science degree, and certify that in their opinion it is worthy of acceptance.

Supervisory Committee

Ahmed M. Hassan, Ph.D., Committee Chair
Department of Computer Science & Electrical Engineering

Ghulam Chaudhry, Ph.D., Department Chair
Department of Computer Science & Electrical Engineering

Deb Chatterjee, Ph.D.
Department of Computer Science & Electrical Engineering

CONTENTS

ABSTRACT iii

LIST OF ILLUSTRATIONS viii

LIST OF TABLES x

LIST OF ACKNOWLEDGEMENTS xi

Chapter

1. INTRODUCTION 1

    1.1 Thesis Outline 4

2. THEORETICAL MODEL 5

    2.1 Method of Moments for Arbitrarily Thin Wires 6

    2.2 The Theory of Characteristic Modes 8

    2.3 Vertical Wire Above A Lossy Half-Space 12

3. DIELECTRIC AND MAGNETIC PROPERTIES OF NANOWIRES AND MICROWIRES 18

    3.1 Metals 18

    3.2 Ferromagnetic Material 20

    3.3 Carbon Nanotube 22

4. GRAPHICAL USER INTERFACE 23

5. RESULTS AND DISCUSSION 27

5.1 Nanowires of Various Metals 27

5.2 Carbon Nanotubes 32

5.3 Ferromagnetic Microwire 36

5.4 Effect of Presence of Lossy Ground 38

5.5 Effect of Multiple Vertical Wires 50

6. CONCLUSION AND FUTURE DIRECTION 53

LIST OF REFERENCES 55

VITA 61

LIST OF ILLUSTRATIONS

Figure Page

1 Model configuration for vertical nanowire above lossy dielectric half-space 5

2 Visualization of approximation of 3D wire into 1D wire with triangular basis function 6

3 Modal Significance plot for a 193nm PEC wire 9

4 Approximation of the first four current modes 10

5 Modal Excitation Coefficient (MEC) for the first three modes of a straight wire.....11

6 Diagram of Green's function contours with poles and branch points 14

7 Relative error between freespace Green's function and modified Green's functions 16

8 Comparison of measured complex electrical permittivity data to Drude Model.....19

9 Comparison of relative permeability for magnetic wire with various DC bias. 21

10 Introductory window of MATLAB graphical user interface. 23

11 Simulation set-up window of MATLAB graphical user interface.....24

12 Simulation results window of MATLAB graphical user interface. 25

13 Validation of scattering cross-section of various lengths of gold wire and Modal Significance plots.....28

14 Extinction cross-sections for straight wires composed of various material.....29

15 Modal Significance plots for Gold, Silver, and Aluminum 30

16 Comparison of Modal Significance, Extinction, and MEC for PEC and Gold wires.....31

17 Extinction cross section and modal significance for CNT with varying relaxation times..33

18 Comparison of Modal Significance, Extinction, and MEC for CNT with varying relaxation time 34

19 Absorbed power for a 9.8 mm Cobalt-rich ferromagnetic wire.....36

20 Extinction cross-section for ferromagnetic wires of varying length.....37

21 Modal Significance plots for various lengths of Co-rich ferromagnetic wire 37

22 Full-wave validation of extinction of gold wire above a substrate 39

23 Extinction cross-section of gold wire above various substrate permittivities.....40

24 Diagram of wire above dielectric half-space showing wire image.....40

25 Extinction cross-section for a gold wire at several heights above a substrate 41

26 Comparison of Modal Significance of a gold wire above PEC and in free-space 41

27 Extinction as a function of angle for a gold wire above substrate with varying permittivity.....42

28 Diagram of wire above substrate and plot of refractive index for varying permittivies.....44

29 First three MEC's for gold wires above PEC, silicon, and in free space.....45

30 Modal Significance, MEC's, and radiation patterns for a gold wire above silicon 46

31 Comparison of extinction cross-section for a gold wire above silicon, gold and in free-space.....46

32 Diagram of dielectric lensing of scattered fields 48

33 Comparison of far-field radiation for a gold wire above various substrate permittivities..48

34 Far-field radiation plots showing radiation beyond critical angle 49

35 Far-field radiation from a gold wire at various heights above interface.....50

36 Simulation model of several wire above an interface, with power absorption plot.....51

37 Simulation model of two wires at different heights above interface and in free-space, with power absorption plots.....52

TABLES

Table Page

1. Drude Model Values for Metals ……...…….....19

2. Magnetic Properties of Co-rich wire ...……..….20

ACKNOWLEDGEMENTS

I would like to express my sincere gratitude to my advisor Dr. Ahmed Hassan for his continuous support and guidance throughout the duration of this work. Besides my advisor, I would like to thank rest of my thesis committee: Dr. Deb Chatterjee and Dr. Ghulam Chaudhry for their encouragement and insightful comments. Also, I would like to thank Dr. Edward Garboczi in the Applied Chemicals and Materials Division at the National Institute of Standards and Technology for his valuable comments and suggestions. This research work was supported by NIST # 70NANB15H285: MSE, "Multi-scale Computational Modeling of Carbon Nanostructures Composites" and NSF # 1629908: CRI, "Experimental Characterization and CAD Development Testbed for Nanoscale Integrated Circuits". Most importantly I would like to thank my dear wife for her love and support, and for helping me to maintain perspective throughout the entirety of this work.

CHAPTER 1

INTRODUCTION

Traditionally, the design of antennas involve structures with resonant wavelengths directly related to their physical length. The simplest example of this is perhaps the dipole antenna, which is theoretically designed such that its resonant wavelengths are multiples of half the overall dipole length, or $L = \lambda/2$. We find, however, that this constant wavelength scaling breaks down for metals at optical frequencies, which Novotny explains in [28]. Previous data, given by Johnson & Christy [19] and others [32, 39], shows that metals typically express very large negative values of relative permittivity at DC and microwave frequencies, that ultimately tend towards zero in the optical regime. The result is that the metals becomes more of a dielectric than a perfect reflector which subsequently allows oscillations of the free-electron gas, resulting in a plasmonic resonance. Furthermore, the significant change in material impedance affects the wave velocity in the wire. One example of this effect is seen in recent work by Kremer's and Chigrin [21], where a straight 300nm gold wire with a 10nm radius is shown to experience electric resonance around 200 THz. This same wire, modeled as a PEC with $\sigma = \infty$, will resonate at approximately 500 THz, where $\lambda \approx 2L$. In the case of the metallic carbon nanotube, the effect is even more significant. The work in [17] shows that a 193nm metallic armchair CNT, with radius $r = 0.61\ nm$, will resonate at approximately 12 THz, where a PEC wire of the same geometry will be expected to resonate at 777 THz. It is characteristics such as this that preclude these materials from being modeled as perfect electric conductors (PEC) at near-infrared and optical frequencies.

The interest in nanowires to design composites with unique electromagnetic properties, optical switches, sensors, detectors, etc. presents a necessity to accurately model their expected

electromagnetic properties [20, 22]. In order to accurately predict the current distribution as well as absorption and scattering characteristics of realistic conductors at optical frequencies, the material properties must be considered for this specific case. This means that the frequency dependent electric permittivity, conductivity, and in certain cases, magnetic permeability must be considered in the analysis. Furthermore, the application of nanowires almost always involves the presence of a dielectric, whether the wire is grown vertically above the substrate, or suspended inside. For this reason, the effects of one or more interfaces on scattering characteristics must also be considered.

To date, significant work has been published on the optical properties of metals and CNT's, as well as the electromagnetic characteristics of nanowires and other nano-structures composed of these materials. It is the understanding of this author, however, that there does not seem to be a comprehensive analysis comparing nanowires of different materials with their electromagnetic characteristics, particularly in layered media. This sort of analysis can be quite useful when attempting to optimize a design solution with the right materials, geometries and excitations. That being said, an analysis comparing the scattering and absorption cross-sections, as well as an in-depth look at current distributions, is performed for various wire materials in the presence of a lossy dielectric interface.

While most software packages offering full-wave solutions provide very accurate results, they often require great computational resources, resulting in long turnaround times on results. In order to reduce computational complexity, we have chosen to use the Method of Moments (MOM) formulation for Arbitrarily Thin Wires (ATW) [10]. This method accurately calculates the electromagnetic response of cylindrical wires with large aspect ratios, or $L > 20r$ and $\lambda \gg r$ [12, 13]. This allows for the three-dimensional (3D) wire to be reduced to a

one-dimensional wire with only an axial component of current. This results in a great savings in computational expenses. Furthermore, to account for the presence of the substrate on which the nanowires are placed, the Green's function describing the environment is modified. By modifying the Green's function, there is no need to mesh the interface, whose dimensions are typically much larger than those of the wire. This results in a further reduction in computational time. Ultimately, developing an efficient electromagnetic model for nanowires, in free space and above an interface, facilitates their use for designing optimum sensors for a variety of applications.

As previously stated, variation in material impedance affects not only the resonance frequency and bandwidth, but it also affects the current distribution and radiation pattern as well. To accurately model and predict the current distribution on the nanowire, we have adapted a current decomposition method based on the Theory of Characteristic Modes (TCM), which was first developed by Garbacz in 1965 [9] and Harrington [14-16]. This method explains the overall current pattern on a conductive body at any particular frequency as an infinite sum of particularly weighted current "modes". Each mode represents a particular current pattern, which contributes to the total current of the nanowire according to its particular weight. The sum of the weighted current modes makes up the overall current density. These individual modes, and their weights, are typically found by solving a weighted eigenvalue equation of the impedance matrix of the conductor, which is explained in [3, 9, 14-16]. Because TCM gives the significance of each mode for a given frequency, one can optimize the wire geometry and material for an ideal current density and radiation pattern. Furthermore, because TCM only needs the impedance matrix as an input, modal significance can be found completely independent of an excitation. That being said, TCM can also be used to explain the

relationship between an incident electric field and current distribution on the wire [6, 17]. This work will show how the material properties of the conductor, and the presence of a lossy dielectric substrate, affect the resonant frequencies of the nanowires, the bandwidths of those resonances and the current distributions at different frequencies. Furthermore, it will serve to help explain why particular current modes are either expressed or not, for certain materials and excitations.

1.1 Thesis Outline

This thesis is organized as follows: Chapter 2 briefly describes the theoretical formulations used for the Arbitrarily Thin Wire approximation, and the Theory of Characteristic Modes, as well as the formulations used to perform simulations on a wire above a lossy half-space. Chapter 3 describes the material properties of certain metals in the terahertz (THz) to optical frequencies, carbon nanotubes, and a ferromagnetic micro-wire using both experimental results and theoretical approximations. Chapter 4 briefly discusses the software implementation of the formulations described in Chapter 2 with the presentation of a MATLAB-based, user-friendly, open-source, software package. Chapter 5 discusses the results of simulation and compares the electromagnetic responses of nanowires of various metals, carbon nanotubes and a ferromagnetic micro-wire, as well as the current modes and modal significance for each wire, in free-space and above an interface. Finally, Chapter 6 will give the conclusion of this thesis and the future directions of the related research.

CHAPTER 2

THEORETICAL MODEL

In this work, our goal is to model the electromagnetic responses of nanowires with various material properties using a computationally efficient model. To accomplish this goal, we chose to use a thin wire approximation as well as a modified Green's function to simplify the simulation meshing. The electrical properties of these nanowires were obtained from reported experimental measurements or from models that fit these experimental measurements. The scope of the work presented in this thesis is restricted to perfectly straight wires excited by plane wave. Analysis is presented for vertical wires floating in free space, and wires vertically oriented above a lossy dielectric half-space.

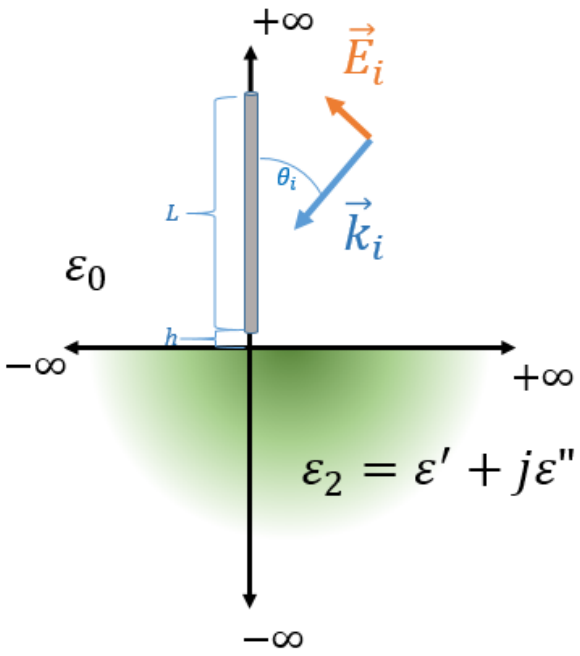

Figure 1 Model configuration for vertical nanowire above a lossy dielectric half-space

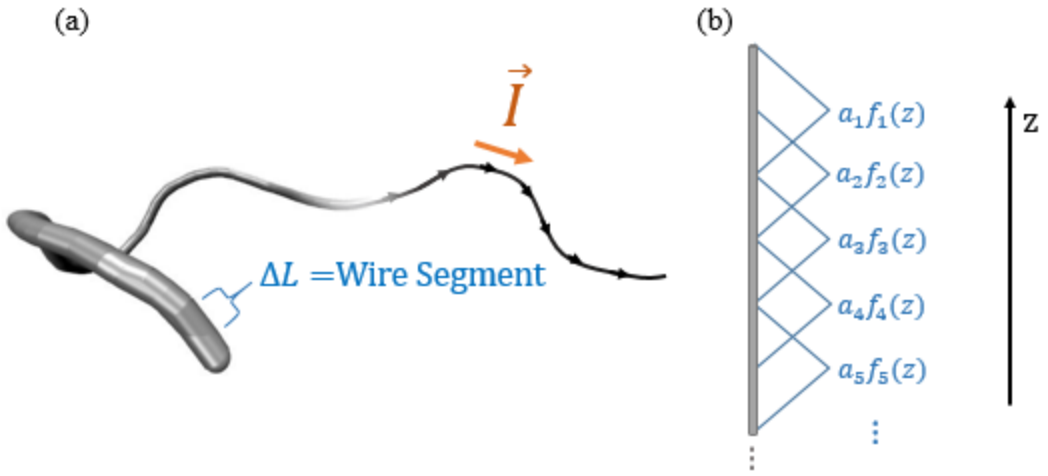

Figure 2 Approximation of 3D wire into a 1D wire, with only an axial current considered (a). Division of wire into triangular basis functions (b).

2.1 Method of Moments for Arbitrarily Thin Wires

To simulate scattering and absorption by the wire, we chose a Method of Moments (MOM) formulation for Arbitrarily Thin Wires (ATW), described by Gibson in [9]. The ATW formulation approximates the 3D cylindrical structure into a 1D wire, assuming only an axial current. The actual wire radius is considered when calculating the distributed impedance of the wire. The 1D wire is then split into segments for the MOM calculation. The sum of the incident electric field, $\vec{E}_{inc}$, and the electric field scattered by the wire, $\vec{E}_{scat}$, is proportional to current on the wire, $\vec{I}(z)$, and its distributed impedance, $\vec{Z}_L$.

$$\vec{E}_{inc} + \vec{E}_{scat} = \vec{I}(z)\overrightarrow{Z_L} \tag{1}$$

Furthermore, the scattered electric field is found through a convolution of the wire current with a transfer function or rather the vector potential for the surrounding medium, as given in the electric field integral equation,

$$-\overrightarrow{E}_{scat}(z) = \frac{j\omega\mu_0}{4\pi}\int_L I(z')G(z,z')dz' \tag{2}$$

The MOM for ATW formulation calculates the total current on the wire through a summation of currents at each segment, by dividing the wire into triangular basis functions.

$$I(z') = \sum_{n=1}^{N} a_n f_n(z) \tag{3}$$

The MOM formulation ultimately results in the following matrix equation:

$$[Z] \cdot \vec{I} = [V] \tag{4}$$

Where [Z] is the MOM impedance matrix, referenced in the next section.

For the ATW approximation to be valid, the aspect ratio of each segment must be such that the length of each segment, L_s, must be significantly larger than the radius of the wire, r. Furthermore, the number of segments, S, must be chosen, such that, for a given excitation frequency, there are at least 20 segments per wavelength. This gives the advised restrictions for the number of segments chosen as,

$$\frac{20L \cdot f_h}{c} < S \lesssim \frac{L}{4r} \tag{5}$$

where L is the overall length of the wire, c is the speed of light in the embedded medium, and f_h is the upper frequency of simulation. Analysis has shown that the accuracy of the frequency response may be improved by increasing the number of segments slightly past the suggested amount. But, as the number of segments is increased, accuracy of the modes/current distribution will start to suffer if the length of each segment becomes smaller than the radius

of the nanowire. Likewise, using less segments will decrease computational time, but the overall accuracy in the results will suffer.

2.2 The Theory of Characteristic Modes

Any conductive object exposed to an alternating electromagnetic field will produce patterns of current on its surface related to its geometry and material properties. Furthermore, these current patterns will vary with the frequency of excitation, polarizability and the direction of the incident wave with respect to this object. The Theory of Characteristic Modes (TCM) states that these current patterns can be expressed as an infinite sum of fundamental current modes that are individually weighted by several factors [9]. This is analogous to the Fourier series expansion of a time-variant function being expressed as an infinite sum of individually weighted sines and cosines. The structure of these current modes and their individual weights can be found by solving the following eigenvalue equation based on the impedance matrix given from the MOM calculation,

$$\mathbf{X}\mathbf{J}_\mathbf{n} = \lambda_n \mathbf{R}\mathbf{J}_\mathbf{n} \tag{6}$$

In the previous equation, **R** and **X** are the real and imaginary parts of the complex impedance matrix, [Z] = $\boldsymbol{Z}$. The eigenvector, $\boldsymbol{J_n}$, represents each current mode, with its weight given by the eigenvalue, λ_n. Because the complex MOM impedance matrix, $\boldsymbol{Z} = \boldsymbol{R} + j\boldsymbol{X}$, is frequency dependent, the current modes and their weights will also change with frequency. From the solutions of (6), we ultimately find that the overall current on a conductive body, for a specific frequency of excitation, can be found from

$$\boldsymbol{J} = \sum_{\boldsymbol{n}=\mathbf{0}}^{\infty} \frac{V_n \boldsymbol{J_n}}{(1+j\lambda_n)\langle \boldsymbol{J_n}, R\boldsymbol{J_n}\rangle} \tag{7}$$

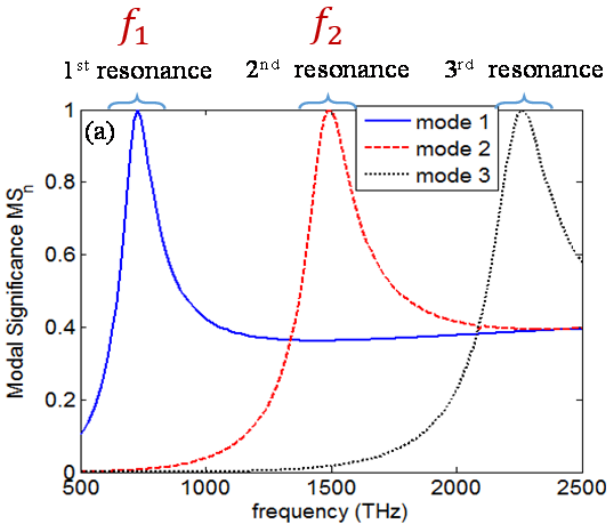

Figure 3 Modal Significance (MS_n) for the first three modes of a perfectly electrically conducting (PEC) straight wire with L=193nm, and r=0.61nm.

$$\langle \mathbf{J_n}, R\mathbf{J_n} \rangle = \int \mathbf{J_n} \cdot (\mathbf{RJ_n}) dl \tag{8}$$

Here we see that the total current density is the infinite sum of each current mode, $\boldsymbol{J_n}$, weighted by several factors. The first being a normalization factor given in (8). The second weighting factor expresses the Modal Significance (MS_n) and is given as a function of the eigenvalue, λ_n, as

$$MS_n = \frac{1}{(1+j\lambda_n)} \tag{9}$$

The Modal Significance tells us how strongly a certain current pattern is expressed at a given frequency. Figure 3 shows a plot of the Modal Significance (MS_n) for the first three modes of a 193 nm perfectly conducting (PEC) straight wire. It is important to emphasize that the MSn is independents of the excitation. Here we see that at the theoretical first resonance, f_1, the first

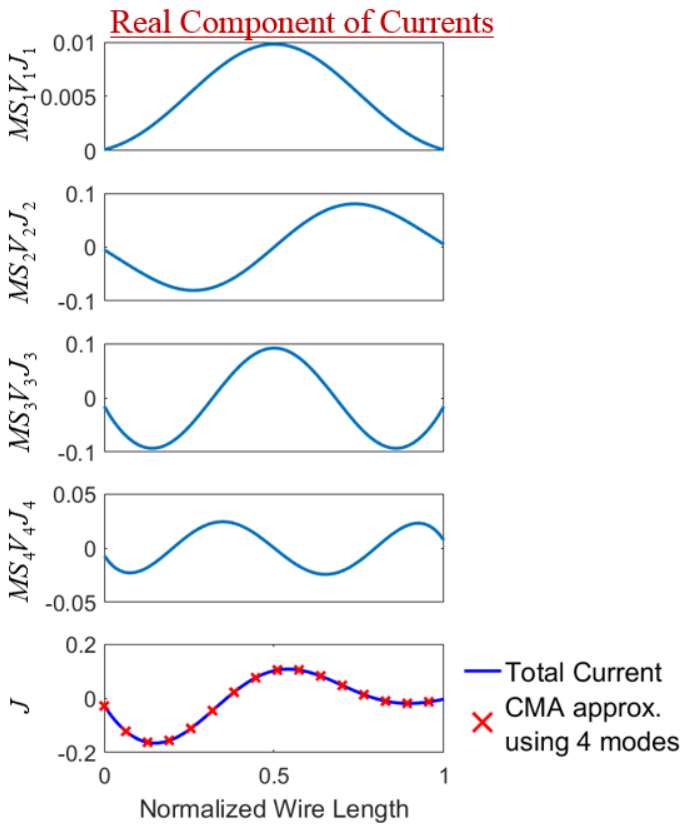

Figure 4 Approximation of the first four current modes and their weighting factors, for a PEC wire, and their summation to produce the total current.

mode is the most significant with almost no contribution from any other mode. At f_2, we find that the overall current is dominated by mode 2 with roughly a 40% contribution from mode 1. This concept is illustrated further in Figure 4, where an approximation of the first four modes for a straight PEC wire is shown with their weighted average.

We see here that each current mode for a wire made of a PEC can be roughly approximated as a sine function of its normalized length,

$$\mathbf{J_n} \approx \sin(n\pi\ell) \tag{10}$$

Where $0 \leq \ell \leq 1$. Up to this point, the orientation of the incident field with respect to the conductor has not been considered. This means that the general modal behavior of a conductive body can be found from its complex MOM impedance matrix, **Z**, alone. We do find, however, that each current mode is further weighted by how strongly it couples with the incident electric field. This is expressed by the Modal Excitation Coefficient (MEC).

$$V_n = \int \mathbf{J_n} \cdot \mathbf{E^i} dl \tag{11}$$

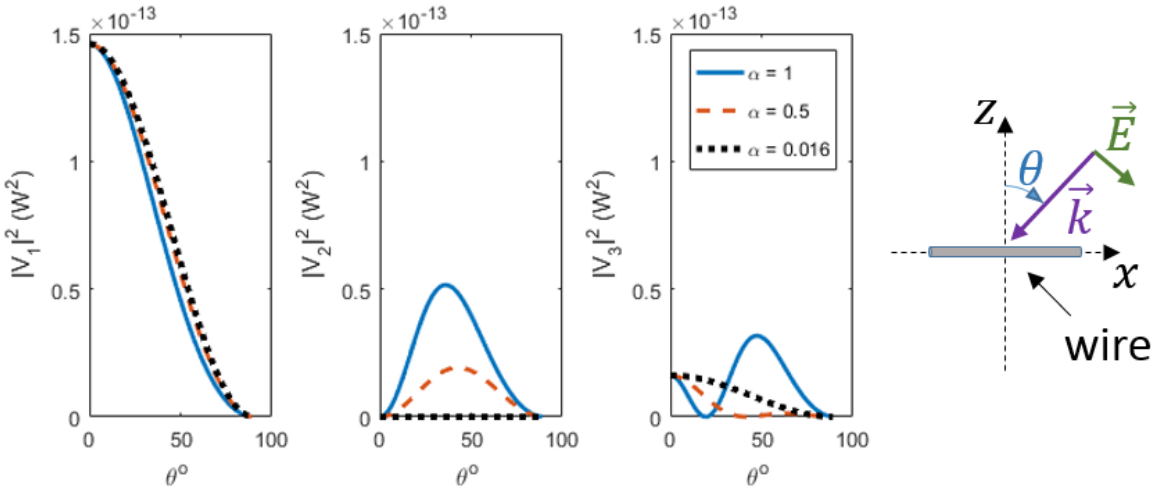

Figure 5 Modal Excitation Coefficient (MEC) for the first three modes of a straight wire with $\mathbf{J}_n = \sin(n\pi l)$, with the incident electric field varying from θ = 0°, to θ = 90°, for α=1, α=0.5, α=0.016.

In the case of the straight PEC wire, using the modal current approximation given in (10), we can approximate the MEC for the first three modes as such:

$$|V_1| = \left(\frac{2L}{\pi}\right)\frac{\cos(\theta)\cos(\varphi)}{[1-\alpha^2\sin^2(\theta)cos^2(\varphi)]}\cos\left[\left(\frac{\pi\alpha}{2}\right)\sin(\theta)\cos(\varphi)\right] \tag{12}$$

$$|V_2| = \left(\frac{L}{\pi}\right)\frac{\cos(\theta)\cos(\varphi)}{[1-\alpha^2\sin^2(\theta)cos^2(\varphi)]}\sin[\pi\alpha\sin(\theta)\cos(\varphi)] \tag{13}$$

$$|V_3| = \left(\frac{2L}{3\pi}\right)\frac{\cos(\theta)\cos(\varphi)}{[1-\alpha^2\sin^2(\theta)cos^2(\varphi)]}\cos[\left(\frac{3\pi\alpha}{2}\right)\sin(\theta)\cos(\varphi)] \tag{14}$$

The previous equations show that the MEC is a function of not only the angle of incidence, but also a velocity factor, α. This velocity factor can be found as a ratio of the first resonant wavelength of the wire under test, to the wavelength of the first resonance of a PEC wire, or $\lambda = 2L$.

$$\alpha = \frac{\lambda_0}{\lambda_{PEC}} = \frac{\lambda_0}{2L} \tag{15}$$

Therefore, in the case of a PEC, $\alpha = 1$. Figure 5 shows plots of the MEC as a function of the angle of incidence for the first three modes a straight wire. From this plot, the effect of the velocity factor α can be seen. In the above figure, the values of α are chosen to compare how several realistic materials will vary in their response to an incident field. In, this case the values of $\alpha = 1, 0.5, and\ 0.016$ are meant to represent a PEC, gold, and a metallic CNT, respectively. We see that, all three appear to share a similar response for the first mode, but begin to differ in subsequent modes. In the case of the CNT, we find that mode 2 will not be expressed at any angle. For mode 3, significant differences exist in the wires of different materials. The implications of the MEC, along with other intrinsic material properties, will be further discussed in Chapter 5.

2.3 Vertical Wire Above a Lossy Half-Space

In general, the electric field scattered from an electrically excited wire can be found through a convolution of the current on the wire with a transfer function, or Green's function, that describes the surrounding medium (2). For the case of free space, the Green's function takes the form of :

$$G(z, z') = \left[1 + \frac{1}{k^2} \cdot \frac{\partial^2}{\partial z^2}\right] g \tag{16}$$

where,

$$g = g_0 = \frac{e^{-jkR}}{R} \tag{17}$$

The Green's function, $G(z,z')$, and the current, $I(z')$, are a function of the source, z', and the observation point, z. The free-space modifier, g_0, is inversely proportional to the radial distance from the source to the observation, $R = \sqrt{(z-z')^2 + r^2}$, and describes how the electric field decays radially from the source in free space.

In the presence of a lossy half-space, however, reflections from and transmission across the interface must be considered. A rigorous derivation of expressions describing this environment has been completed by Sommerfeld in 1909 [40], and has been subsequently developed by Miller, and Sarkar [28, 37]. Sommerfeld's main contribution, in this case, is the following equivalence, now known as the Sommerfeld identity.

$$\frac{e^{-jkR'}}{R'} = \int_0^\infty J_0(\lambda r) e^{-\sqrt{\lambda^2 - k_1^2}(z+z')} \frac{\lambda}{\sqrt{\lambda^2 - k_1^2}} d\lambda \tag{18}$$

In this expression, $R' = \sqrt{(z+z')^2 + r^2}$, and describes the radial distance from the source image, caused by reflections from the interface, to the observation point. Sarkar points out that the expressions for the fields above the interface and below can be achieved by multiplying the integrand of (18) by a reflection coefficient, $R(\lambda)$, and a transmission coefficient, $T(\lambda) = 1 - R(\lambda)$, respectively, where:

$$R(\lambda) = \frac{\varepsilon_2\sqrt{\lambda^2 - k_1^2} - \varepsilon_1\sqrt{\lambda^2 - k_2^2}}{\varepsilon_2\sqrt{\lambda^2 - k_1^2} + \varepsilon_1\sqrt{\lambda^2 - k_2^2}} \tag{19}$$

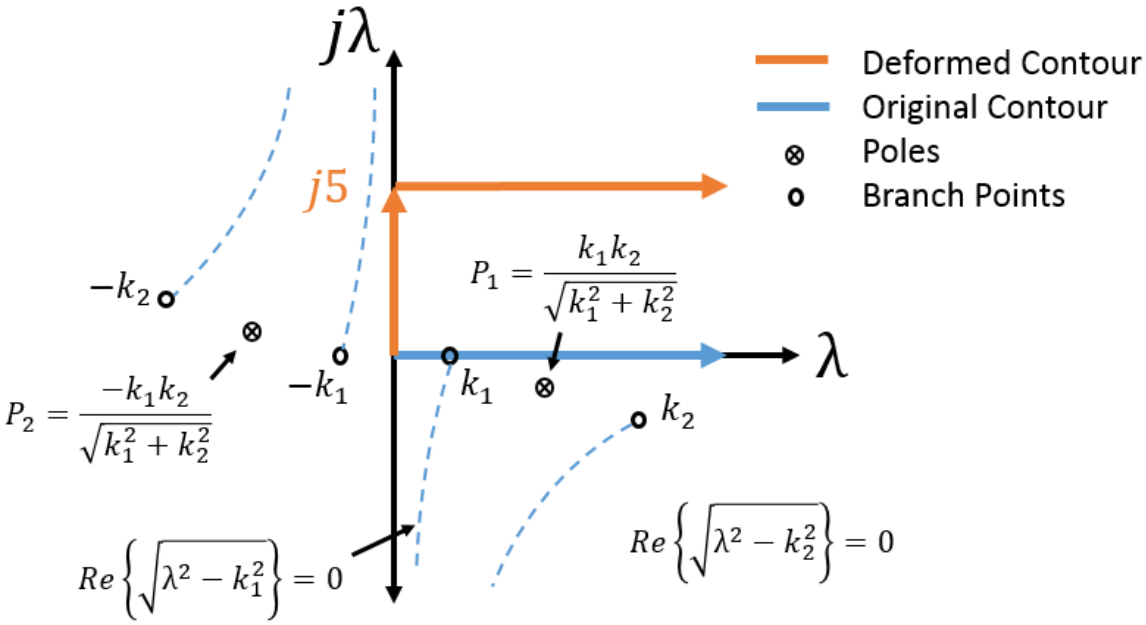

Figure 6 Diagram of contours with poles and branch points

In the specific case of a vertical wire above an infinite lossy half-space, the Green's functions for fields above the interface, g_1, and below the interface, g_2, are given by Sarkar in the following forms:

$$g_1 = g_0 + g_r =$$

$$\frac{e^{-jkR}}{R} + \int_0^\infty J_0(\lambda r) e^{-\sqrt{\lambda^2-k_1^2}(z+z')} \frac{\varepsilon_2\sqrt{\lambda^2-k_1^2}-\varepsilon_1\sqrt{\lambda^2-k_2^2}}{\varepsilon_2\sqrt{\lambda^2-k_1^2}+\varepsilon_1\sqrt{\lambda^2-k_2^2}} \cdot \frac{\lambda}{\sqrt{\lambda^2-k_1^2}} d\lambda \qquad (20)$$

and,

$$g_2 = 2\int_0^\infty J_0(\lambda r) e^{-z\sqrt{\lambda^2-k_2^2}-z'\sqrt{\lambda^2-k_1^2}} \frac{\lambda}{\varepsilon_2\sqrt{\lambda^2-k_1^2}+\varepsilon_1\sqrt{\lambda^2-k_2^2}} d\lambda \qquad (21)$$

where g_r is a reflection term that accounts for the imperfect reflections from the interface. $k_1 = \omega\sqrt{\varepsilon_1}$ and $k_2 = \omega\sqrt{\varepsilon_2}$ are the wave-numbers in the upper and lower half-spaces, respectively. Direct calculation of these integrals are complicated by the presence of branch points, and poles on the contour, as shown in Figure 6. Miller and Sarkar show that all branch points and poles lie in the second and fourth quadrants. Therefore, by deforming the contour in the first quadrant, these branch points and poles can be avoided. The particular deformation used in this work, and shown in Figure 6, follows the method given by Sarkar in [37]. Sarkar's analysis shows that all poles and branch-points can be avoided by integrating into the positive imaginary plane from 0 to j5, then continuing the contour integration from the point, (0, j5) to real positive infinity. For example, the reflection term will take the form,

$$g_r = \frac{e^{-jkR'}}{R'} - 2j\int_0^5 \frac{I_0(\lambda a)e^{-j\sqrt{\lambda^2+k_1^2}(z+z')}}{\varepsilon_2\sqrt{\lambda^2+k_1^2}+\varepsilon_1\sqrt{\lambda^2+k_2^2}}\frac{\sqrt{\lambda^2+k_2^2}}{\sqrt{\lambda^2+k_1^2}}\lambda d\lambda -$$

$$2\int_0^\infty \frac{J_0(\beta a)e^{-\sqrt{\beta^2-k_1^2}(z+z')}}{\varepsilon_2\sqrt{\beta^2-k_1^2}+\varepsilon_1\sqrt{\beta^2-k_2^2}}\frac{\sqrt{\beta^2-k_2^2}}{\sqrt{\beta^2-k_1^2}}\beta d\lambda \qquad (22)$$

Where $I_0(\lambda a)$ is the modified Bessel function of the first kind, and $J_0(\beta a)$ is the zeroth order Bessel function of a complex argument, where $\beta = \lambda + j5$. The transmission term, g_2, can also be handled with the same deformation and takes a similar form to (22).

From this point, the integral calculations were achieved using the global quadrature integration method native to MATLAB. To validate the calculation of these integrals, the modified Green's functions, g_1 and g_2, were calculated for the case of $(\varepsilon_1 = \varepsilon_2 = 1)$, where

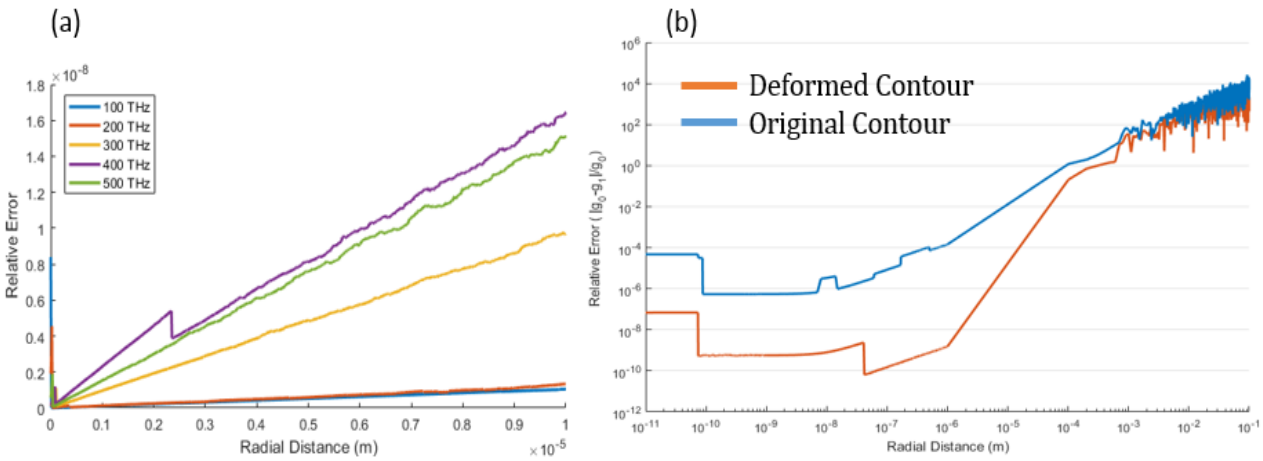

Figure 7 Relative error between the MATLAB calculation of free-space Green's function and the modified Green's functions for the case of $\varepsilon_1 = \varepsilon_2 = 1$ for the deformed contour at radial distance from 1nm to 10um, with respect to frequency (a), and both contours at radial distance from 10pm to 10cm at 500 THz (b).

the solution should be equal to the free-space Green's function, $g_0 = \frac{e^{-jkR}}{R}$. Figure 7a shows the relative error between the modified Green's functions for the case of ($\varepsilon_1 = \varepsilon_2 = 1$) and the free-space Green's function for this case. Multiple frequencies are shown in Figure 7a and the general trend is that the error increases as the frequency increases. Incidentally, the native "integral" function in MATLAB can handle the original contour, but at the expense of relative error several orders of magnitude greater than that of the deformed contour. We see that the general trend from Figure 7b is an increase in the relative error with vertical distance, (z+z'). In this research, the vertical distances considered were relatively small, so the amount of relative error involved was acceptable. Note that calculation by this method is only valid for $z + z' \neq 0$. To calculate the specific case of $z + z' = 0$, alternate methods must be employed, as the integrand of (18) will suffer from poor convergence. Calculation of the

integrals in (22) at values very close to zero, however, reveal acceptable error (Fig 7b), and are considered a valid approximation.

For the consideration of radiation in the far-field we referenced the work by Engheta *et al.* [7], which gives the far-field radiated power density in W/m^2 for the fields above and below the interface. These are denoted by S_{r1} and S_{r2}, for a vertical dipole directly on the interface, respectively as:

$$S_{r1} = \frac{I_o^2}{8\pi^2}\sqrt{\frac{\mu_0}{\varepsilon_0}}\frac{n^4 k_1^2 \sin^2\theta \cos^2\theta}{\left(n^2 cos\theta + \sqrt{n^2 - \sin^2\theta}\right)^2}\frac{1}{r^2} \tag{23}$$

$$S_{r2} = \frac{I_o^2}{8\pi^2}\sqrt{\frac{\mu_0}{\varepsilon_0}}\frac{n^5 k_1^2 \sin^2\theta \cos^2\theta}{\left(n\sqrt{1 - n^2\sin^2\theta} - cos\theta\right)^2}\frac{1}{r^2} \tag{24}$$

I_0 is the individual current element on the wire, $n = \sqrt{\varepsilon_2}$ is the refractive index of the lower half-space, and r is the radial distance from the source. These approximations are only valid for current elements located on the surface of the interface. To account for current elements at varying heights above the interface, we referenced the work by Lukosz and Kunz in [24, 25], which gives scaling factors to account for the change in height.

CHAPTER 3

DIELECTRIC AND MAGNETIC PROPERTIES OF NANOWIRES AND MICROWIRES

To obtain impedance profiles for the materials included in this thesis, measurements from multiple references were considered [19, 32, 39, 42]. To allow for flexibility in frequency range and selection when performing simulations, theoretical models were ultimately utilized to fit the experimentally measured frequency dependent relative permittivity, permeability, and impedance. The following sections of this chapter describe the models used, and their respective references. Validation of these theoretical models has been completed in the works with which they have been referenced [2, 30]. However, a comparison of measured data for certain metals with the proposed theoretical model is given in the following section.

3.1 Metals

The experimentally measured frequency dependent electrical permittivity for the metals was approximated by the Drude Model approximation used in [2] and [21], and takes the form,

$$\varepsilon(\omega) = \varepsilon_{\infty} - \frac{\omega_p^2}{\omega^2 + j\gamma\omega} \tag{25}$$

where ω is the angular frequency of incident radiation, and the plasmon frequency, ω_p, and the relaxation time, γ, are unique to each material. The parameter ε_{∞} is a corrective term for $\omega \gg \omega_p$ and represents the effective permittivity of each metal as $\omega \to \infty$. The associated Drude Model values for each of the metals are given in [2] and are summarized in Table I. The agreement between the Drude model approximations and experimental data for gold, silver,

Table 1 Drude Model Values for Metals

Material	ε_∞	ω_p	γ
Gold	9	$1.36674 \times 10^{16}\ s^{-1}$	$7.59297 \times 10^{13}\ s^{-1}$
Silver	6	$14.585 \times 10^{15}\ s^{-1}$	$34.6393 \times 10^{12}\ s^{-1}$
Aluminum	1	$23.245 \times 10^{15}\ s^{-1}$	$90.9129 \times 10^{13}\ s^{-1}$
Sodium	1	$8.675018 \times 10^{15}\ s^{-1}$	$41.9318 \times 10^{12}\ s^{-1}$
Potassium	1	$5.6517 \times 10^{15}\ s^{-1}$	$27.9545 \times 10^{12}\ s^{-1}$

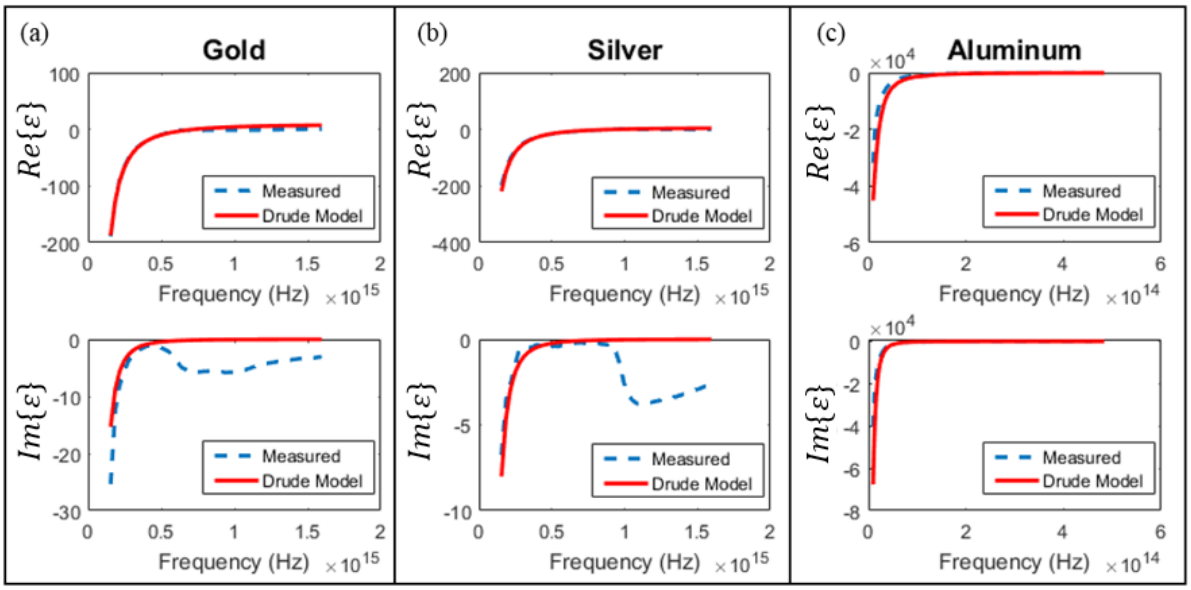

Figure 8 Comparison of measured complex electrical permittivity data to Drude Model approximation for (a) Gold, (b) Silver, (c) and Aluminum [2]. Measured data is taken from [19] for gold and silver, and [32] for aluminum.

and aluminum can be found in Figure 8. Note that this approximation is agreeable up to 500 THz for most materials, and even higher for some specific cases. The distributed impedance, defined as the impedance per unit length of the wire, is calculated using an expression based on cylindrical Bessel functions of wavenumber, k, and radius, r, given in [23] as,

$$Z_L = \frac{j\eta}{2\pi r} \cdot \frac{J_0(kr)}{J_0'(kr)} \tag{26}$$

where $\eta = \sqrt{\frac{j\omega\mu}{\sigma + j\omega\varepsilon}}$, and $k = \omega\sqrt{\mu\varepsilon}$ represent the impedance of the medium and propagation constant inside the wire, respectively. The parameter J_0 is the zeroth order Bessel function of the first kind, and J_0' is its derivative. All of the metals simulated in this work were assumed to be non-magnetic and are given a relative permeability of $\mu_r = 1$.

3.2 Ferromagnetic Material

For the case of the ferromagnetic wire, we referred to the work in [23] where the magnetic permeability of the material is based on typical ferromagnetic properties for cobalt, which are given in Table 2. For this case, the relative electric permittivity is expressed purely from the electric conductivity as $\varepsilon = -j\sigma/\omega$. The distributed impedance of the wire was then calculated from (23). A unique characteristic of the ferromagnetic wire is the possibility of a

Table 2 Magnetic Properties of Co-Rich Wire

Constant	Value	Property
γ	$2 \cdot 10^{11} T^{-1} s^{-1}$	Gyro-magnetic ratio
$\mu_0 M_s$	$0.55\ T$	Saturation magnetization
σ	$5 \cdot 10^5\ S/m$	Conductivity
α	0.02	Magnetic losses factor
H_{eff}	$95\ kA/m$	DC magnetic field

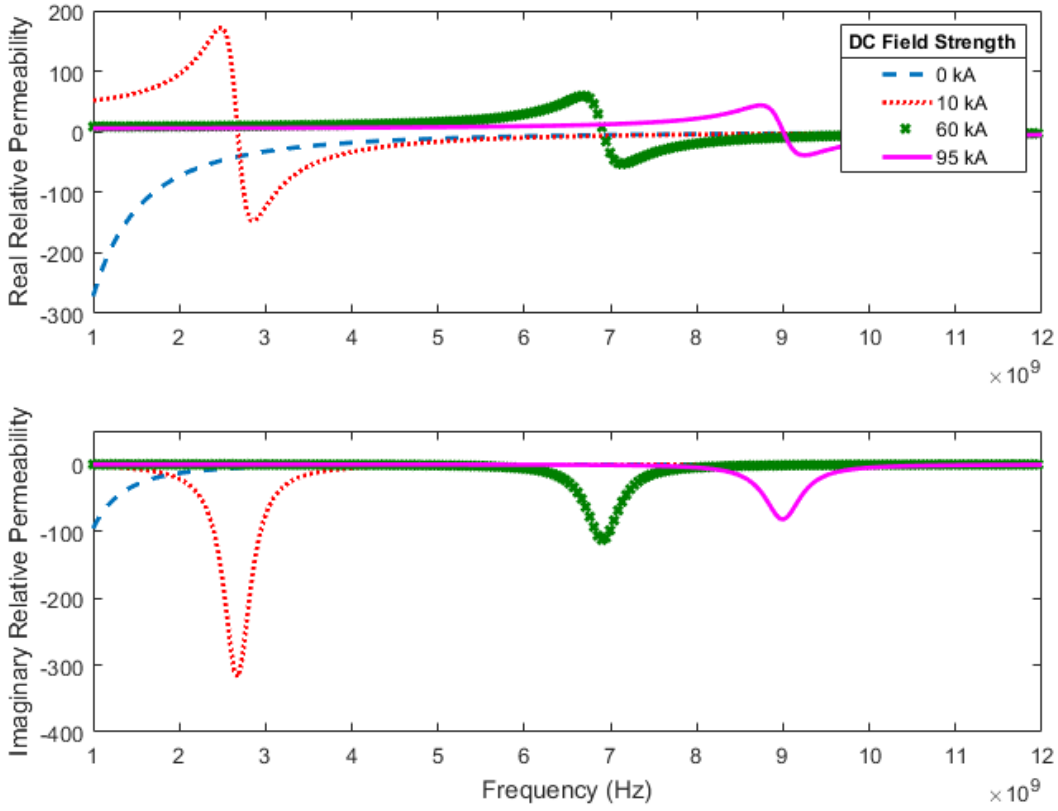

Figure 9 Comparison of complex relative permeability for ferromagnetic wire with varying strengths of DC magnetic field bias.

Ferromagnetic Resonance (FMR) associated with an applied DC magnetic field, H_{eff}. Figure 9 shows the complex relative permeability for the ferromagnetic wire in the presence of a DC magnetic field bias of varying strength. We see that the frequency of the FMR is proportional to the magnetic field strength. For the simulations contained in this thesis, the field strength of 95 kA/m was maintained, giving an FMR of approximately 9 GHz. The effects of this resonance and its impact on electric resonance are discussed in Chapter 5.

3.3 Carbon Nanotube

To simulate the carbon nanotube (CNT), we referred to the work in [17] to approximate the axial conductivity of a metallic single-walled carbon nanotube (SWCNT). The following expression for Drude model conductivity of a SWCNT was utilized,

$$\sigma_{CNT} = \frac{\sigma_0}{1+j\omega\tau} \tag{27}$$

$$\sigma_0 = \frac{2e^2 v_F \tau}{\pi^2 \hbar r} \tag{28}$$

where e is the electron charge, v_F is the Fermi velocity, ħ is the normalized Plank's constant, and τ is the relaxation time. It should be noted that this model is only valid at frequencies below the inter-band transitions for metallic CNT's with chirality indices, $(n, m) < 50$. In this work, the (9, 9) armchair CNT was exclusively modeled with a radius $r = 0.61nm$ and Fermi velocity $v_F = 9.71 \times 10^5 m/s$. The relaxation time was varied between $\tau = 0.03ps$ and $\tau = 3ps$ to cover the range of reported values in the literature. It is possible that this wide range in τ stems from differences in sample quality affecting the individual reports of calculated relaxation time. It is likely that impurities in the CNT lattice would cause an increase in the electron collision frequency, and inversely, reduce the relaxation time, τ. For this reason, an analysis on how scattering is affected by changes in this value is performed. The distributed impedance for the previous model can be found as a function of the Drude conductivity and the CNT chirality, or subsequently, its radius r.

$$Z_{CNT} = R_{CNT} + j\omega L_{CNT} = \frac{1}{2\pi r \sigma_{CNT}} \tag{29}$$

CHAPTER 4

GRAPHICAL USER INTERFACE

The theoretical models and associated calculations outlined in previous chapters were performed by computation in MATLAB. To simplify the simulation setup and to create a means of accessibility to the simulation by others, a graphical user interface was designed and integrated with all the associated MATLAB scripts to create an open source software package titled “Scattering and Modal Analysis of Conductive Nanowires.” This package is currently designed in two flavors, wires in free space and wires in the presence of a lossy half-space. The foremost software package allows the user to select any arbitrary wire geometry, as well as several common geometries, the number of segments to be used in the MOM calculation, material impedance, and also the desired excitation. The latter program, considering a wire in

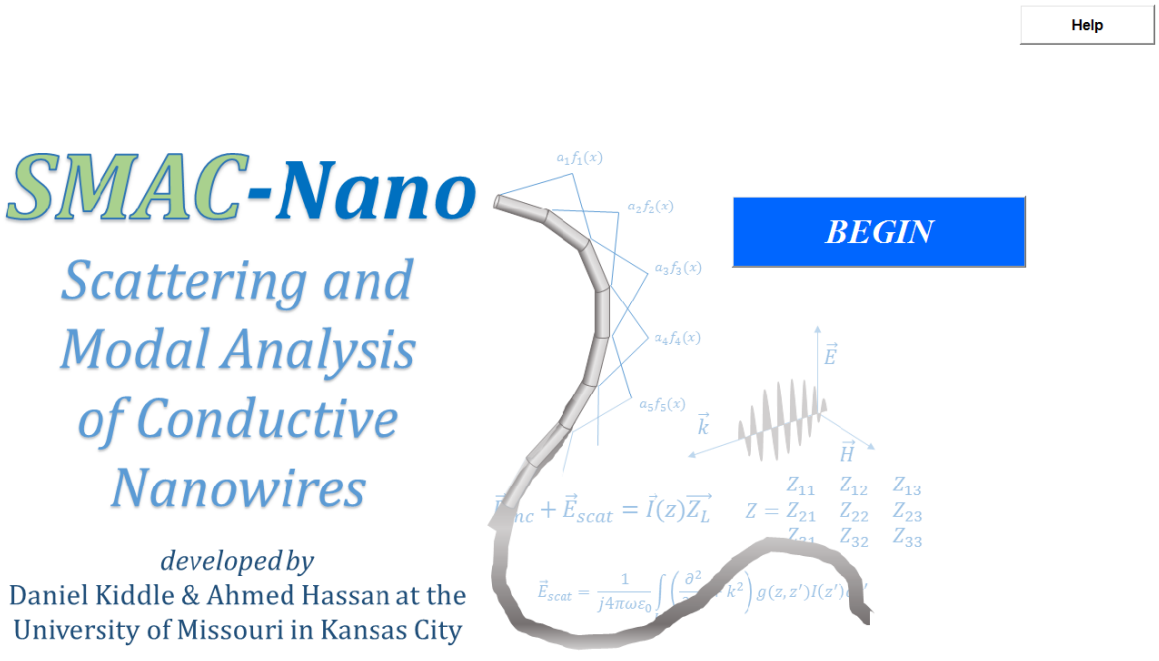

Figure 10 Introductory window of GUI for MATLAB based software package, SMAC-Nano.

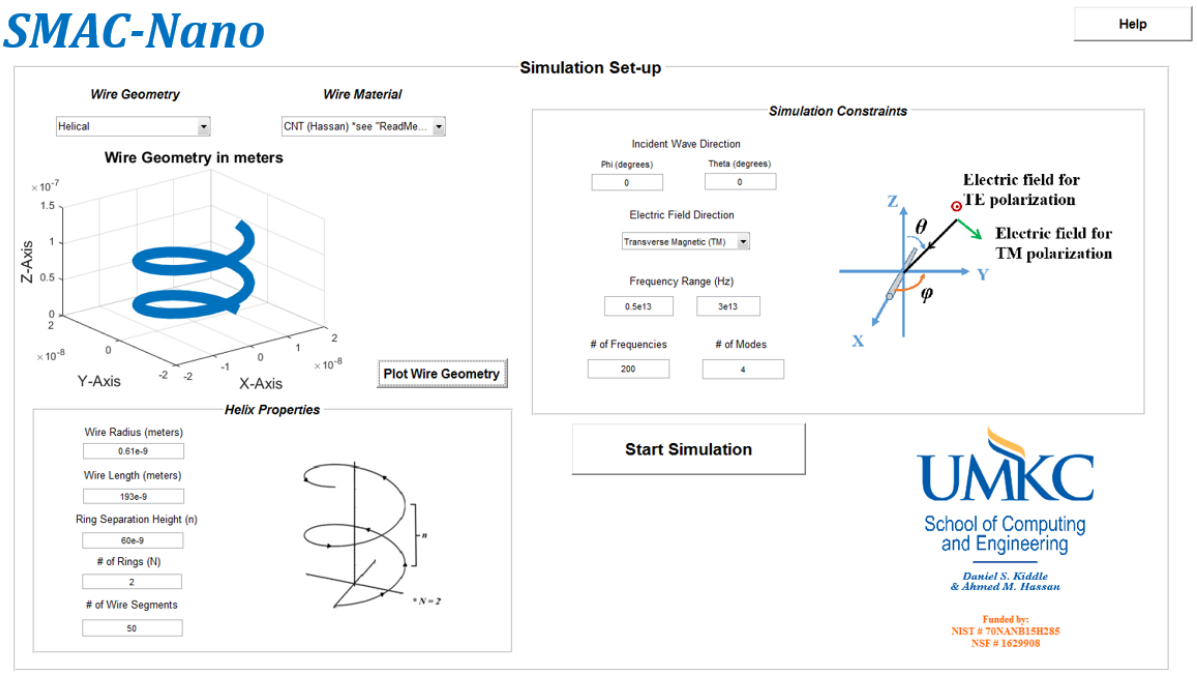

Figure 11 Simulation set-up window of GUI for MATLAB based software package, SMAC-Nano.

the presence of a lossy dielectric half-space, contains options for boundary location with respect to the wire, as well as dielectric properties of both half-spaces. This package currently only supports calculations for a perfectly straight wire orthogonal to the interface, but future work will expand this to account for an arbitrarily shaped wire.

As previously stated, the free-space package offers three common wire geometries to choose from: straight, helical, and c-shaped. The user may also define their own geometry by importing the appropriately formatted 3-D matrix. For the lossy half-space package, the default is the geometry for a vertical straight wire. Wire material properties are available as either Drude model approximations or experimental data. The reason for including the Drude model approximations was to allow for valid simulations outside of the frequency range of the

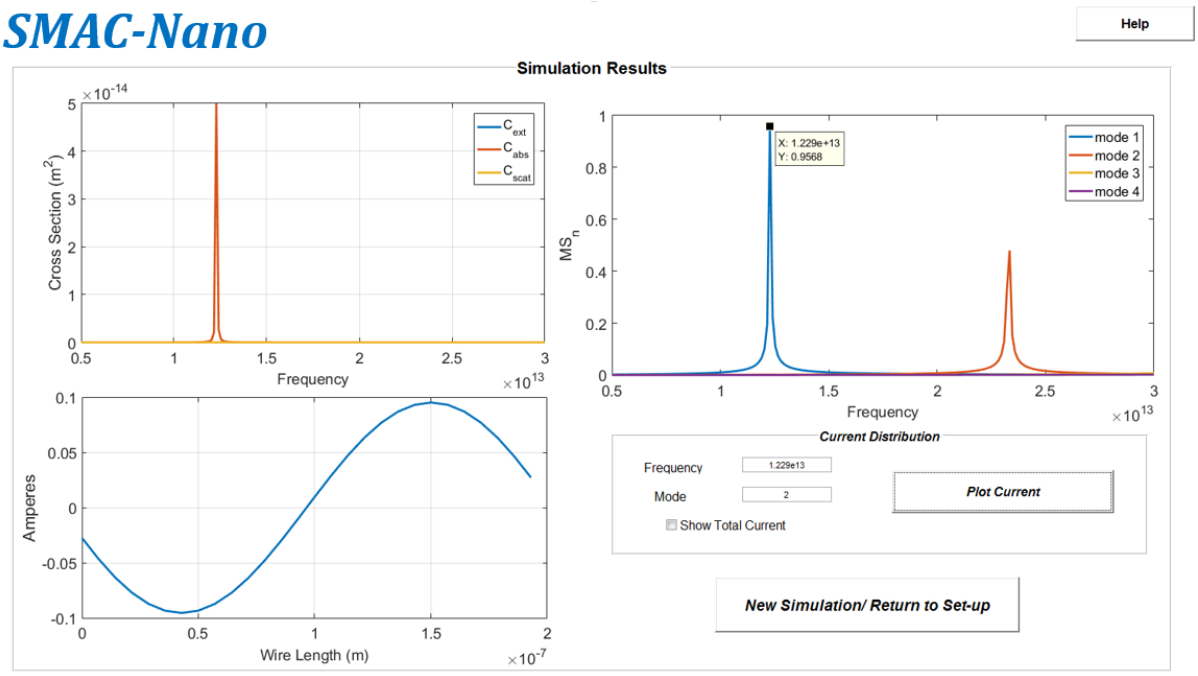

Figure 12 Simulation results window of GUI for MATLAB based software package, SMAC-Nano.

experimental data, and also to provide a comparison for validity. Both packages offer selections for the wire materials covered in this work as well as others. For the lossy half-space package, a constant value for the complex relative permittivity of both half-spaces may be chosen, or several frequency dependent selections can be made for metals or a doped silicon based on the work in [42]. Any user-defined permittivity vector may be input as well to define either half-space. For both packages, choices on excitation include angle of incidence, polarization, frequency range, number of frequencies, and the number of modes calculated.

The outputs of the packages are a plot of the extinction cross-section, absorption cross-section, and scattering cross-section, with respect to the selected frequencies. The modal significance over the selected frequency range is also plotted for the number of modes chosen. The user may also choose to plot the total current, or any of the calculated current modes at

any of the frequencies included in the simulation. The package will also write the majority of these outputs to files within the current directory. As previously stated, these packages are open-source and can be augmented for many different purposes and applications.

CHAPTER 5

RESULTS AND DISCUSSION

The initial efforts of our analysis were first to validate the MOM for ATW formulation realized by our MATLAB scripts with 3D full-wave simulations performed by either ourselves, or found in published work. This was followed by simulations of a straight wire in free-space to relate the material properties of the wire to their electromagnetic resonances and resonance bandwidths. This then lays the foundation for the characteristic mode analysis, which explains how the material properties of the wire affect its current structures and coupling with the incident EM field. The same analysis is finally extended to the case of a vertical wire in the presence of a lossy half-space. The effects of excitation angle and the half-space dielectric properties are then examined. Finally, our analysis is expanded to a brief introduction into the effect of multiple wires in close proximity.

5.1 Nanowires of Various Metals

Validations were first carried out for the gold nanowire model by comparing the scattering curves for various wire lengths reported in [21]. This work was chosen as a primary reference mainly because of it's rigorous nature, but also because the gold wires modeled were of suitable aspect ratio to simulate with the thin wire approximation used in this work. The work in [21] consists of comparisons of several rigourous numerical methods including HFSS for finite-element frequency-domain, ANSYS for time-domain, and ADDA for discrete dipole approximation .These are also compared with semi-analytical 1-D integral equation methods based on Pocklington-like equations. Gold wires with lengths from 50nm to 300nm, and a 10nm radius were modeled which allowed for various aspect ratios to validate our thin wire approximation. Excellent agreement was found between the published simulations and the

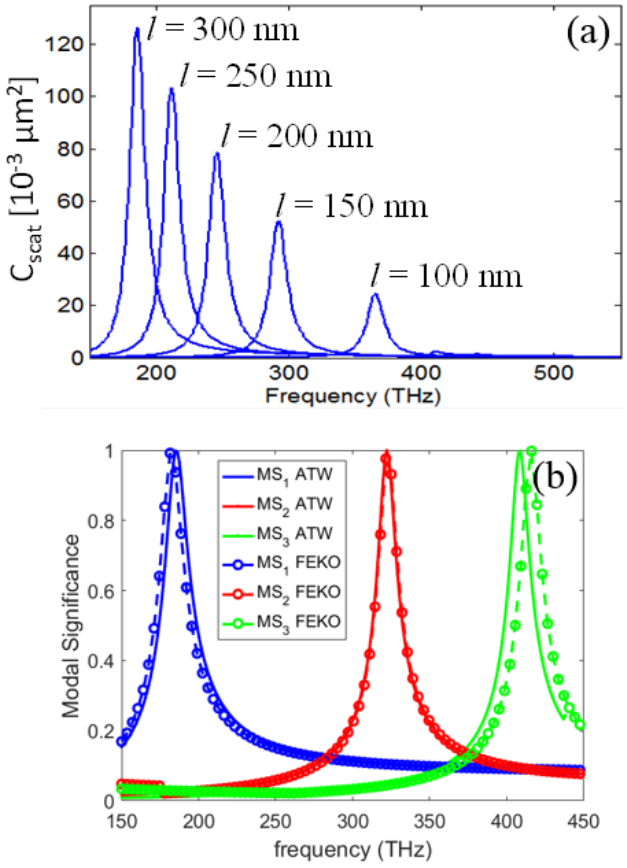

Figure 13 (a) Scattering cross-section for various lengths of gold nanowire with radius, r =10nm using MOM for ATW formulation. (b) Modal significance for a gold wire with length, L = 300nm, and radius, r = 10nm. Dashed line shows Feko simulation and full line shows ATW approximation.

MOM for ATW formulation, which can be seen by comparing Figure 13a with the reported results in [21]. Figure 13a shows the extinction cross-section with respect to frequency when the incident electric field is perfectly parallel to the wire. The extinction cross-section represents the sum of the absorption and extinction cross-sections and can be considered as the total electromagnetic response of the wire for a given excitation. These initial validations were followed with an in-house, 3D, full-wave simulation in FEKO, for the modal significance of the first three modes of a 300nm gold wire with a 10nm radius. Agreement between our FEKO simulation and the MOM for ATW simulation can be seen in Figure 13b. We found that slight deviation in modal resonance began increasing at higher

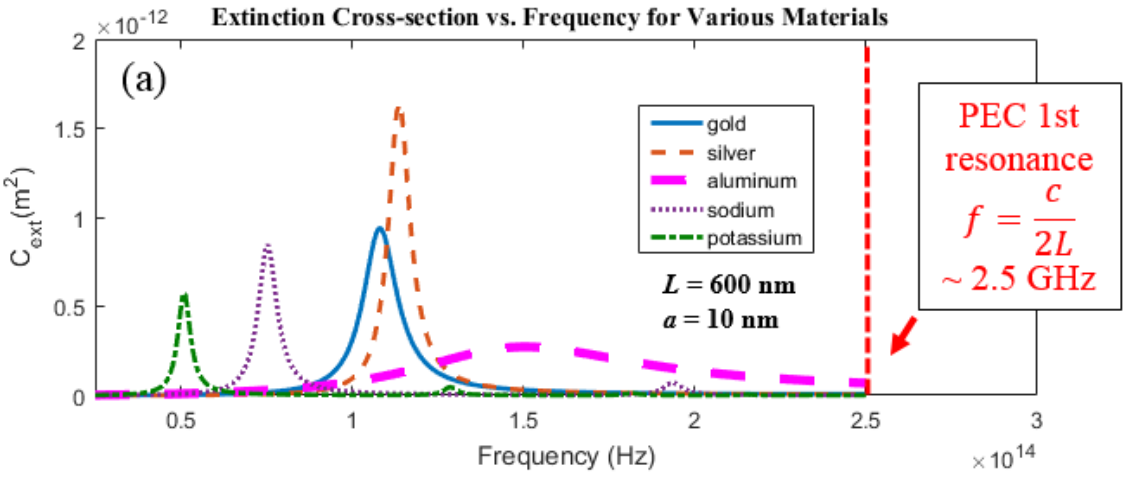

Figure 14 Extinction cross-section for straight wires of various materials, with L = 600nm, and r = 10nm.

frequencies. This is due to the breakdown of the ATW formulation as the wavelength of the excitation approaches the segment length. As was noted in Section 2.1, an increase in the number of segments can decrease this error, but will impact the accuracy of the current distribution calculation.

We then expand our simulations to include silver, aluminum, potassium, and sodium. As explained in Section 4.1, this is done by changing the values of the Drude model for electric permittivity in accordance with Table I. For the bulk of the analysis on the metals covered in this work, a 600nm wire with a 10nm radius is modeled with the electric field component of the excitation completely parallel to the wire. Immediately apparent is the differences in resonant frequency for wires of the same geometry but various complex permittivity. A comparison of the extinction cross-section with respect to frequency in Figure 14 shows how the first electric resonance can be tuned by varying the distributed impedance in the wire.

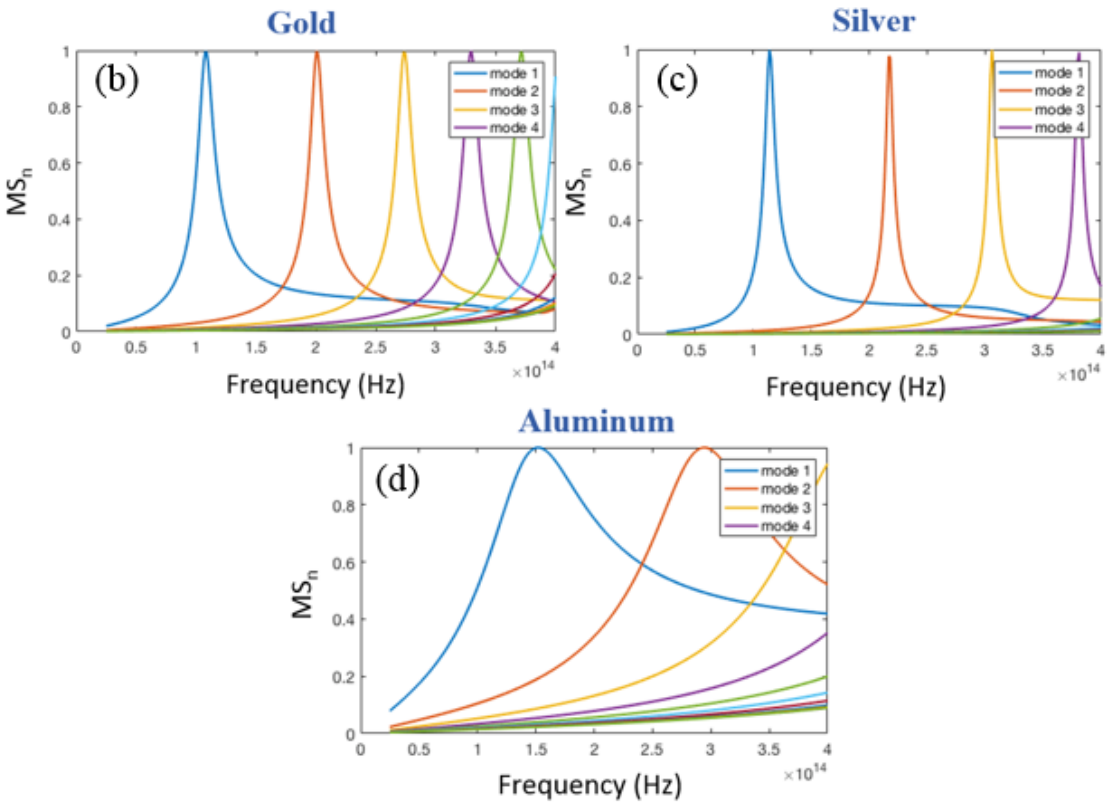

Figure 15 Modal Significance (MS_n) for gold (b), silver (c), and aluminum (d) wires of the same geometry.

Furthermore, plots of the modal significance for the first four modes for Gold, Silver, and Aluminum in Figure 15 show distinct differences in modal overlap and resonance bandwidth. We see that while the overall extinction for aluminum is lower than gold or silver, the current distribution may also be very different. At its second resonance, silver and gold share less than a 0.2 weighted contribution from mode 1 with the majority of the overall current structure being dominated by mode 2. In Aluminum, however, mode 1 contributes a much higher weight, close to 0.5. This means that the current distribution at the second resonance will be different for aluminum than it will be for silver and gold because it will be composed of a different combination of weighted modes.

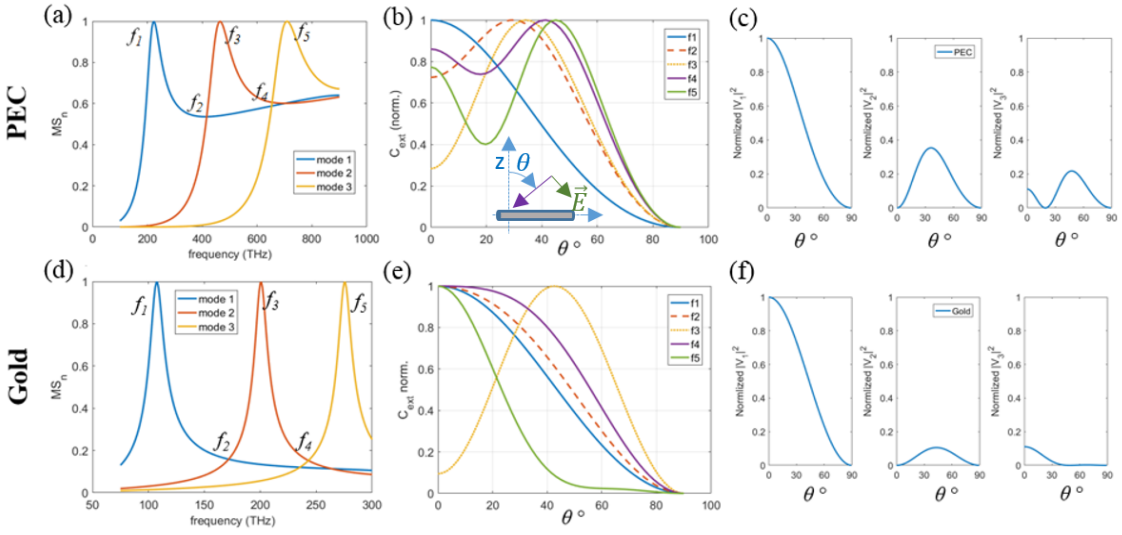

Figure 16 The top row shows (a) the modal significance, MS_n, (b) the angle-dependent normalized extinction cross-section for several frequencies, and (c) the angle dependent modal excitation coefficient curve for modes 1, 2, and 3, all for the case of a PEC with L = 600nm, and r = 10nm. The bottom row shows the same plots, respectively (d-f), for a gold wire of the same geometry.

As we know from Section 2.2, the overall current distribution is weighted not just by the modal significance but also by the modal excitation coefficient, or the coupling between the incident field and the mode. This means that the angle of incidence will further affect the overall current distribution in the wire. Figure 16 shows a comparison between PEC and gold wires of the same geometry. In this analysis, the modal significance (Figure 16a, d) is shown next to a plot of the normalized extinction cross-section with respect to angle of incidence (Figure 16b, e). Next to that is a plot of the modal excitation coefficient (MEC) for the first three modes (Figure 16c, f). Recall from Section 2.2 that the MEC is a function of the velocity factor, α. If we start with the MSn for the PEC wire (Figure 16a), we see that, at f_1, mode 1 is completely dominant, meaning that the normalized extinction cross-section curve for f_1

(Figure 16b) should resemble the first MEC curve, or $|V_1|^2$ (Figure 16c). At f_2, however, both mode 1 and mode 2 share equal significance, meaning that the normalized extinction cross-section for f_2 should be a super-position of the first two MEC curves for the PEC wire. At f_3 we see that mode 2 is dominant with a lesser contribution from mode 1. As before, we see this ultimately reflected in the extinction cross section curve. Following the same steps for the gold wire, we see that it will couple differently with the incident field leading to differences in radiation pattern compared to the perfectly conducting wire. At f_1 both the gold and PEC wires share similar extinction curves due to the similarity in their mode 1 MECs. However, at f_2 we find that the lower mode 2 MEC maximum for the gold wire results in the extinction curve for the gold wire more closely following the mode 1 MEC curve, as opposed to the extinction curve for the PEC wire, which more closely resembles a mixture of its mode 1 and mode 2 MECs. At f_5, we see that the difference in mode 3 MECs between the gold and PEC wires results in very different extinction curves at that frequency.

5.2 Carbon Nanotubes

The analysis of the SWCNT in this work was considered to be an extension of the similar work in [17], in which the MOM for ATW formulation has been validated with full-wave simulation. The focus of the analysis on the metallic SWCNT is two-fold. The first is on the effects of relaxation time, and the second follows the same analysis as for the metals, the effect on modal significance and coupling with the incident field. As previously stated, the wide range in the published relaxation times for the metallic CNT has prompted an analysis on

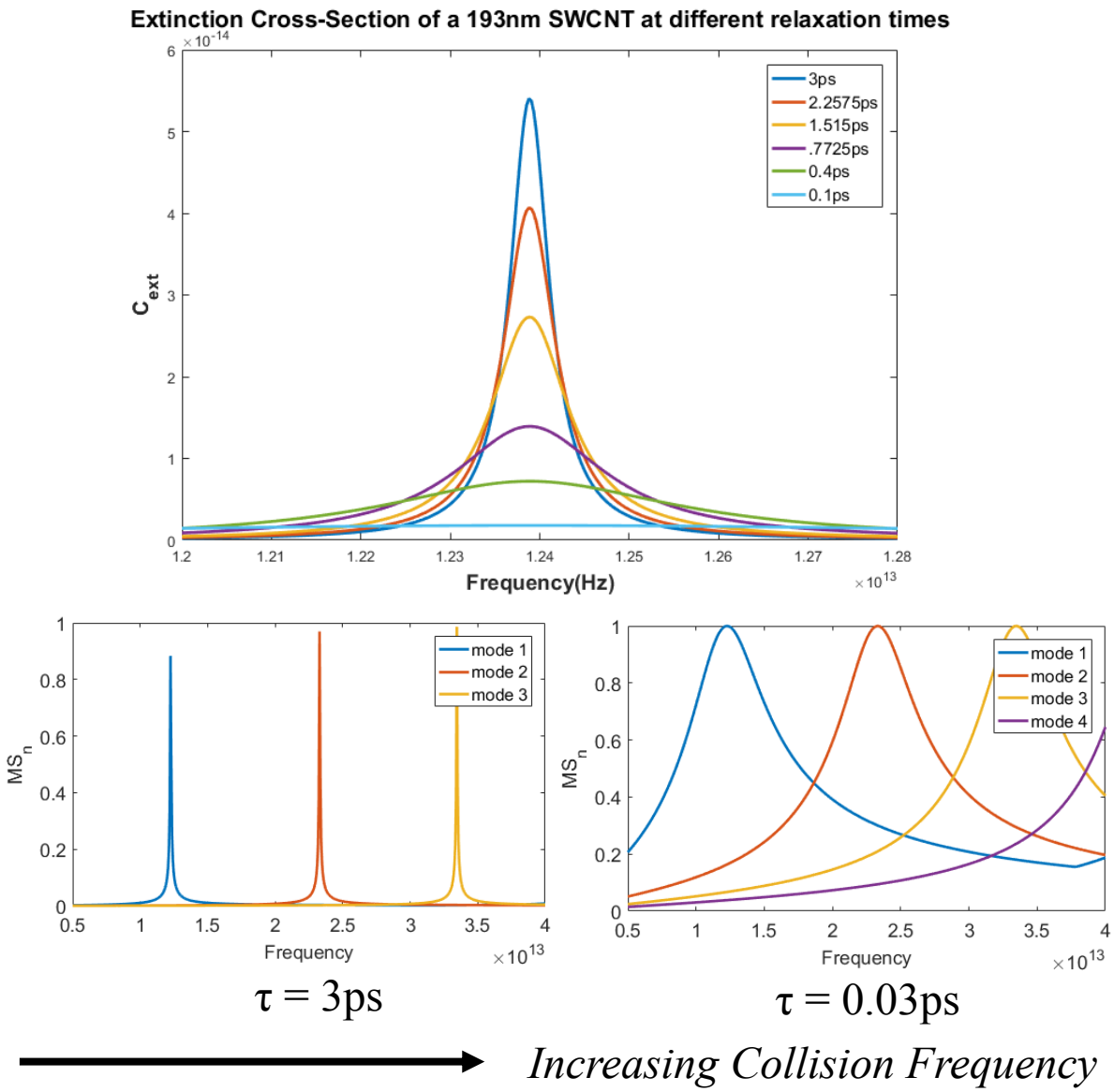

Figure 17 (top) Extinction cross-section, and (bottom) Modal Significance, for metallic SWCNT for varying values of relaxation time, τ.

the effect of changes in this value. As it turns out, varying this value has a significant effect on the electrical behavior of the SWCNT in the presence of EM excitation. From the Drude model approximation discussed in Section 3.3, we find that the ohmic losses in the wire are a function of relaxation time, τ, given by the following expression:

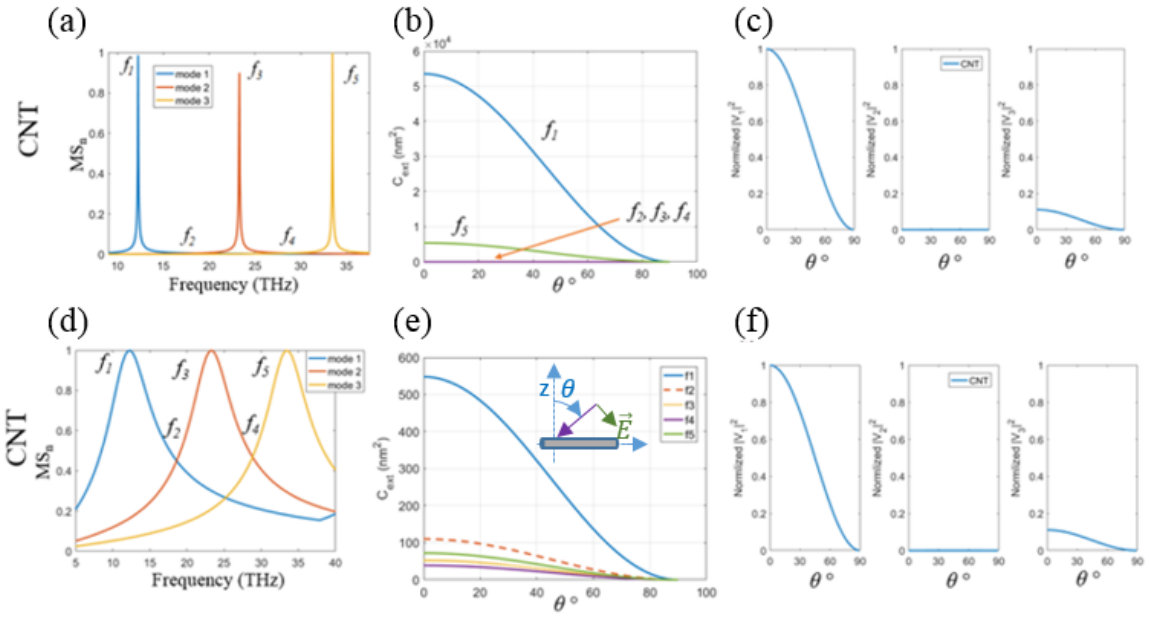

Figure 18 Comparison of Modal significance (a, d), angular dependent extinction cross-section (b, e), and angular dependent MEC, $|V_n|^2$ (c, f), for a (9, 9) SWCNT with τ = 3ps (top) and τ = 0.03ps (bottom).

$$R_{CNT} = \frac{\pi\hbar}{4e^2 v_F \tau} \tag{30}$$

The relaxation time is the inverse of the frequency of collisions of electrons in the CNT lattice. The impact of this is mainly on the bandwidth of the electric resonances and the modal overlap. From Figure 17 we see that a lower collision frequency is associated with a much smaller bandwidth, or higher quality factor (Q). But as the frequency of collisions are increased, so are the ohmic losses, leading to a much larger bandwidth. Furthermore, we see that an increase in collision frequency increases the modal overlap, affecting the current distributions and ultimately the radiation pattern. Comparing the Modal Significance plots for the CNT in Figure

17 with the Modal Significance curve for the PEC wire of the same geometry in Figure 1, one might expect that as the relaxation time continues to increase, or as $\tau \to \infty$, the Modal Significance curves for the CNT should approach that of the PEC wire. We find this is not the case simply because the inductance of the CNT remains unchanged with respect to relaxation time, while the inductance for the PEC is exactly zero. This results in the characteristic quality factor for the CNT that is only decreased by ohmic losses.

Figure 18 shows a similar comparison to that of the analysis of Figure 16 where, instead of comparison to the PEC, we compare two cases of relaxation time. Several main differences should be noted in these plots. The first of which, is that, as opposed to the normalized extinction cross section curves of Figure 16b and 16e, for this analysis we have chosen to retain the original magnitudes in Figures 18b and 18e. This is to impact the difference in coupling with the incident field that a CNT shows compared to other conductors. This leads to the second difference, which is that the MEC for the second mode of a metallic SWCNT in Figures 18c and 18f is zero over all angles of incidence, and for the third mode it is very similar in behavior to the first modal MEC, but its magnitude is much less. This means that although we see a full contribution of mode 2 and 3 at f_3 and f_5 in Figures 18a and 18d, respectively, we find that only the first resonance is strongly expressed in the CNT. This is more the case for the CNT with a 3ps relaxation time (Figure 18a), where the modal separation is greater. We see that because the mode 2 MEC is zero over all angles, and because it is the only significant mode at f_3, there is no coupling with the electric field at any angle for that frequency. This is also true at f_2 and f_4 because there is no modal contribution at those frequencies. At f_5 however, mode 3 couples weakly with the electric field, resulting in much less overall extinction. When the relaxation time is decreased to 0.03ps, as in Figure 18d, we see that the

increase in bandwidth results in mode 1 coupling with the electric field over a larger frequency range. This is why considerable extinction is still seen at f_2 and f_3.

5.3 Ferromagnetic Microwire

Our analysis of ferromagnetic wire follows the work in [23], and utilizes the same simulation conditions, which is a Cobalt-rich wire, 9.8mm long with a 22.5um radius, unless otherwise noted. This allows for validation of our application of the MOM for ATW formulation for wires with very large aspect ratios and a far infrared frequency regime. Results were compared with [23] for validation. Perhaps the most interesting attribute of the ferromagnetic wire is its Ferromagnetic Resonance (FMR). This resonance is related to the field strength of a DC magnetic field applied parallel to the wire axis and is a function of the ferromagnetic properties of the material. The plot of absorbed power versus frequency in Figure 19 shows the FMR centered at approximately 9 GHz followed by the first electric resonance at approximately 15 GHz in the case of radius $r = 22.5\mu m$.

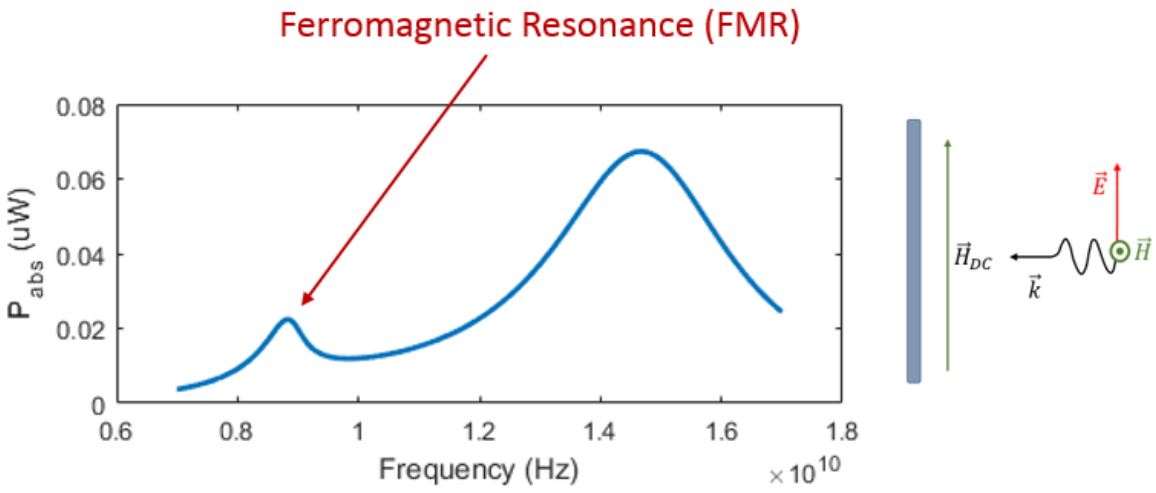

Figure 19 Absorbed power for a 9.8mm Co-rich ferromagnetic wire with a radius, $r = 22.5\ \mu m$

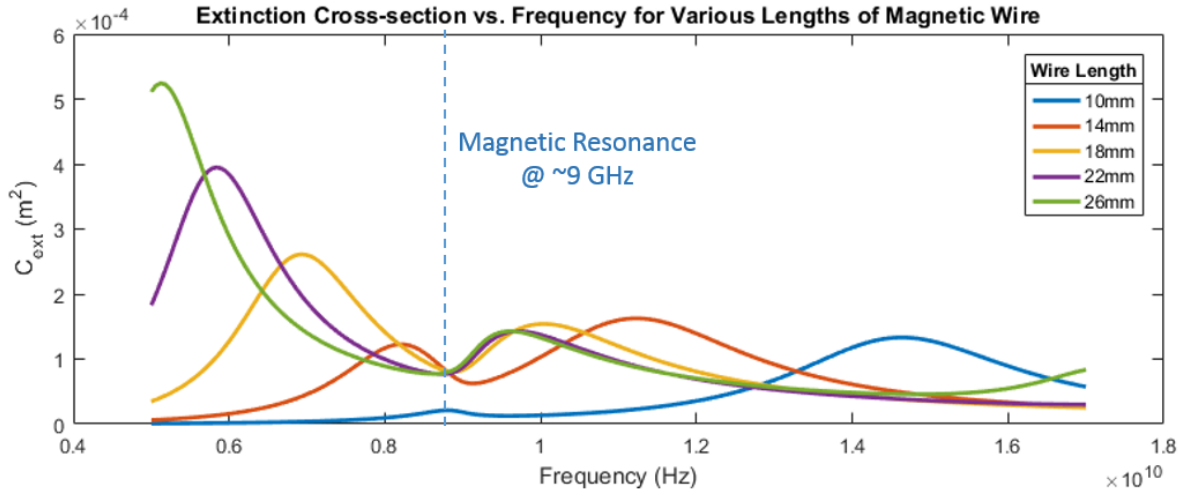

Figure 20 Extinction cross-section of various lengths of Co-rich ferromagnetic wire with radius $r = 22.5\mu m$.

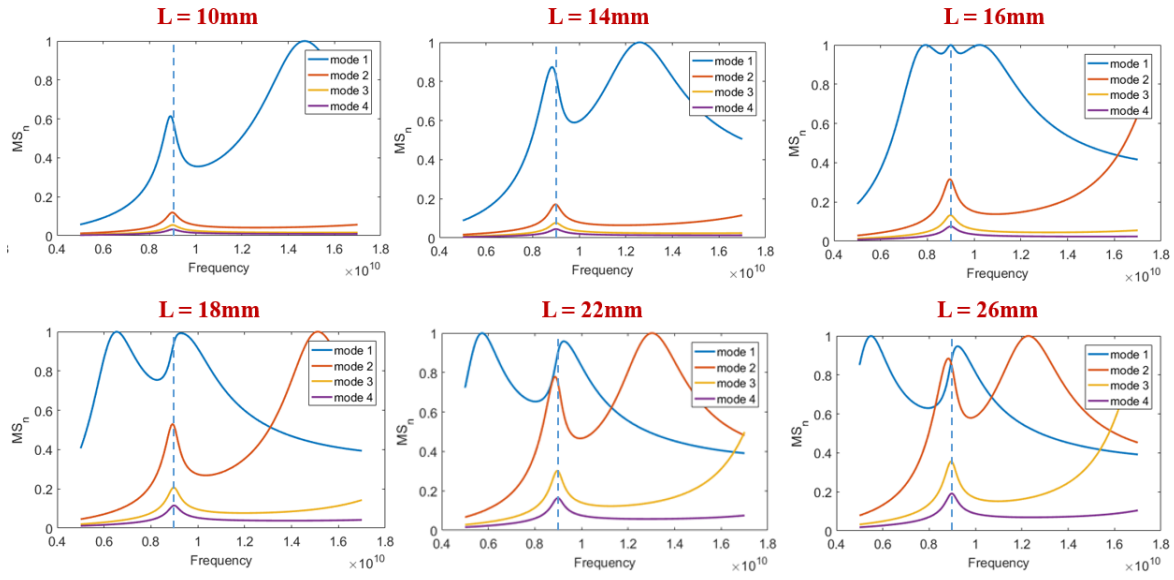

Figure 21 Modal significance plots for various lengths of Co-rich ferromagnetic wire, with the FMR notated by the dotted line.

Of particular initial interest was investigation into how the extinction curve would behave as the electric resonance was made to coincide with the FMR. To simulate this, multiple wire lengths were considered to track the electric resonance moving down in frequency,

passing over the static magnetic resonance. The effects of this can be seen in Figure 20 and Figure 21. What we find is some interference between the two resonances resulting in the appearance of a cancellation of the two resonances at that frequency. The plots of Modal Significance for various length of wire, in Figure 21, reveals that the FMR remains near 9 GHz while the electric resonance continues to shift down in frequency, proportional to wire length.

5.4 Effect of Presence of Lossy Ground

As expressed in Section 2.3, the conductive wire excited in the presence of a dielectric boundary presents some unique effects to be considered. The first of which is the effect the impedance of the lossy half-space has on the resonant frequency of the wire and the next is the effect it has on coupling with the incident field, and the radiation patterns above and below the interface.

Preliminary analysis of the wire above an interface first involves validating our implementation of the modified Green's function in our MOM code by comparing it with a 3D full-wave simulation in FEKO. We chose to use the same 600 nm gold wire model from the previous sections, and simulated the wire at a height of 1 nm above the interface. The reason for this height selection, is mainly because the integrand in the modification term of the Green's functions (20, 21) will not converge if the wire is exactly on the interface, or rather when $z + z' = 0$. This is a common computational problem plaguing multiple EM solvers. The more practical reason, however, is that in reality a nanowire grown vertically on a substrate will almost never actually be in perfect contact with the interface, due to methods of fabrication [20] . For these reasons, a height of 1 nm was considered to be a sufficient approximation for our analysis. Our initial validation considered the gold wire above two substrates. The first was a lossless dielectric with a relative permittivity of $\varepsilon_r = 4$. The second was modeled as a doped

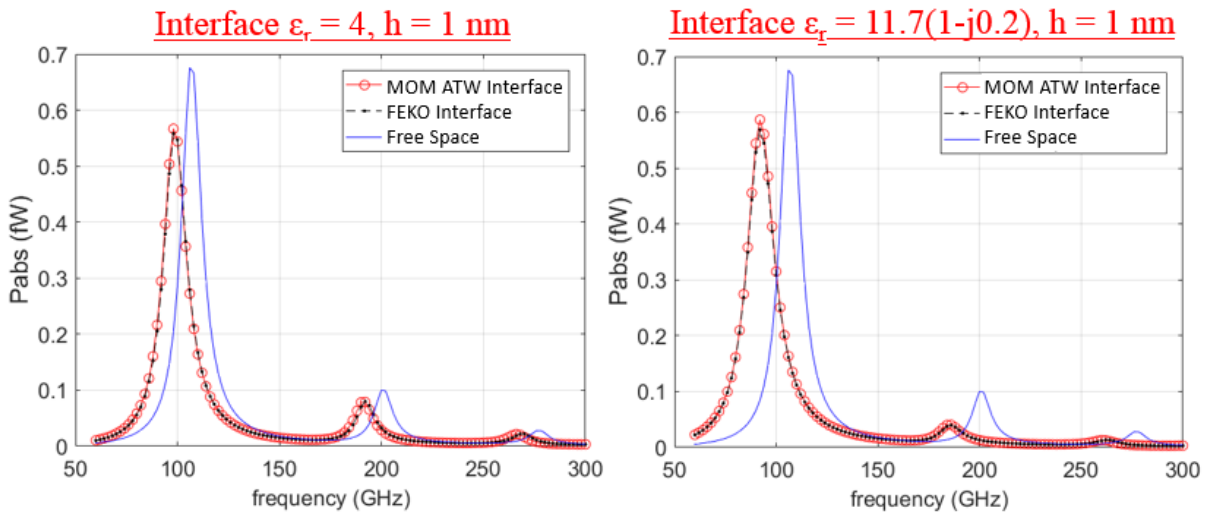

Figure 22 Extinction cross-section for a 600nm gold wire 1 nm above a dielectric infinite half-space with (left) $\varepsilon_r = 4$, and (right) $\varepsilon_r = 11.7(1 - j0.2)$, compared with gold wire in free-space

silicon with a relative permittivity of $\varepsilon_r = 11.7(1 - j0.2)$. As can be seen in Figure 22, agreement was quite excellent for these two cases.

If we expand our analysis of the gold wire to include varying magnitudes of relative permittivity, we can see that the general trend is that resonant frequency of the wire is inversely proportional to the magnitude of relative permittivity in the half-space (Figure 23). This is due to a virtual increase in electric length from the wire image in the half-space. We see that an increase in permittivity results in an increasingly reflective interface. This results in a decrease in the impedance of the image. From the diagram of Figure 24 we see how this change in image impedance also affects the mutual capacitance between the wire and its image. The decrease in image impedance creates an increase in mutual capacitance, resulting in a decrease in resonant frequency. Conversely, as the height of the wire above the interface increases, or the permittivity of the dielectric decreases, we see that the mutual capacitance decreases, resulting

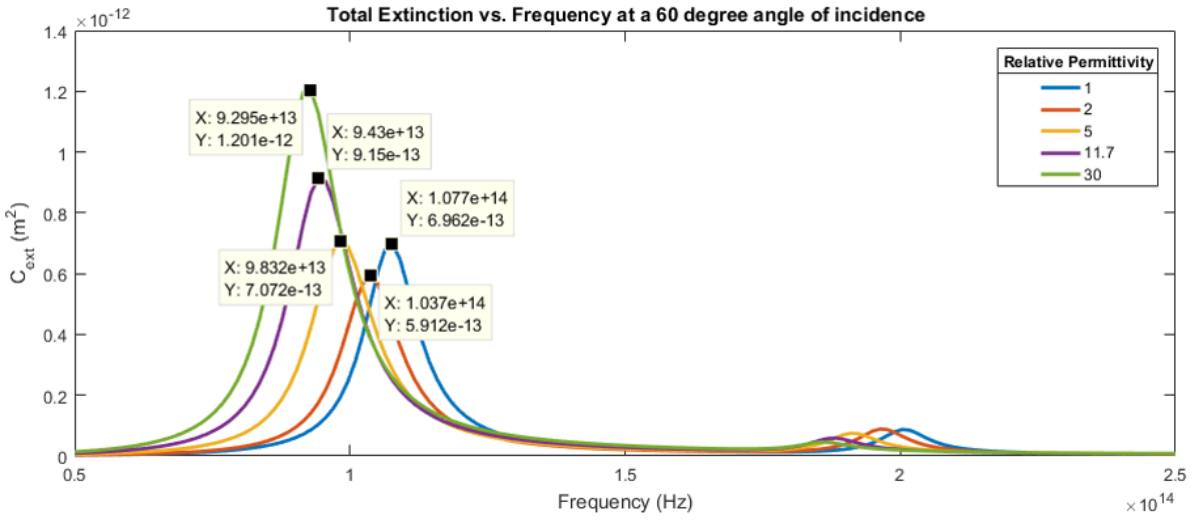

Figure 23 Extinction cross-section for a 600nm gold wire 1 nm above a dielectric infinite half-space with varying magnitudes of relative permittivity.

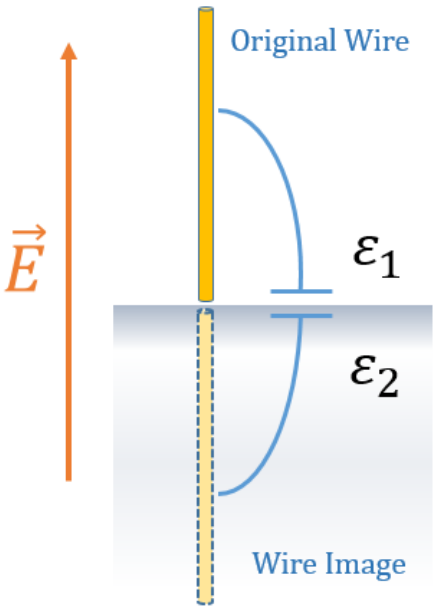

Figure 24 Model diagram for wire above lossy dielectric half-space showing the original wire above and its virtual image below.

in an increase in resonant frequency. The results of the effect of height is shown in Figure 25, where a 600 nm gold wire is modeled above silicon. Comparing the curve for the gold wire at a 10 nm height in Figure 25 with the same wire in free space from Figure 22, we also see that the resonant frequency of the wire quickly converges towards the free-space case with only a small distance from the interface.

From the curves in Figure 2, we see that there is no significant change in the relative bandwidth of the modes for the cases shown. To explore this further, we consider the Modal Significance plots for two limiting cases. Figure 26 shows the Modal

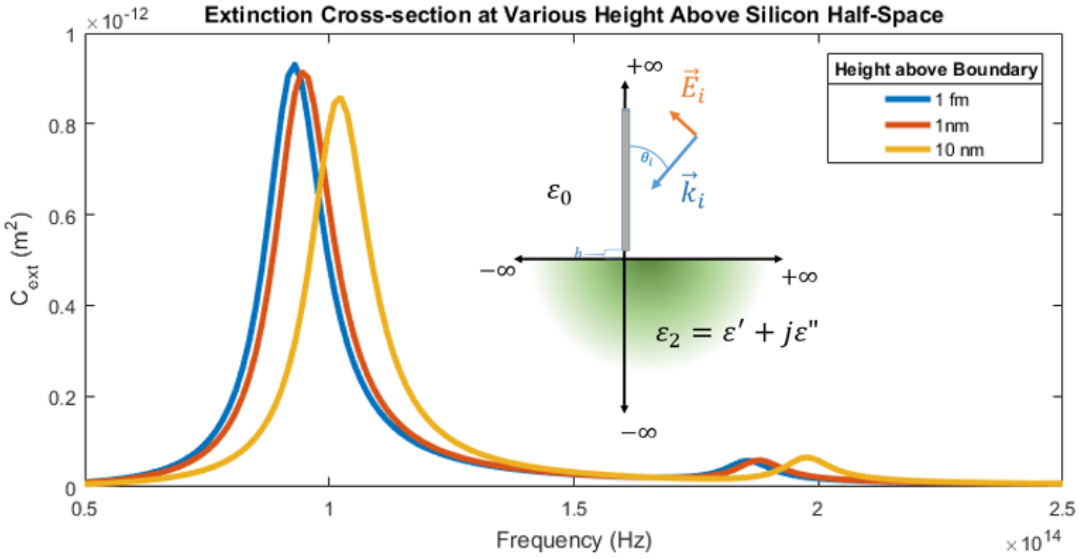

Figure 25 Extinction cross-section for a 600nm gold wire at several heights above a silicon interface with $\varepsilon_r = 11.7(1 - j0.2)$.

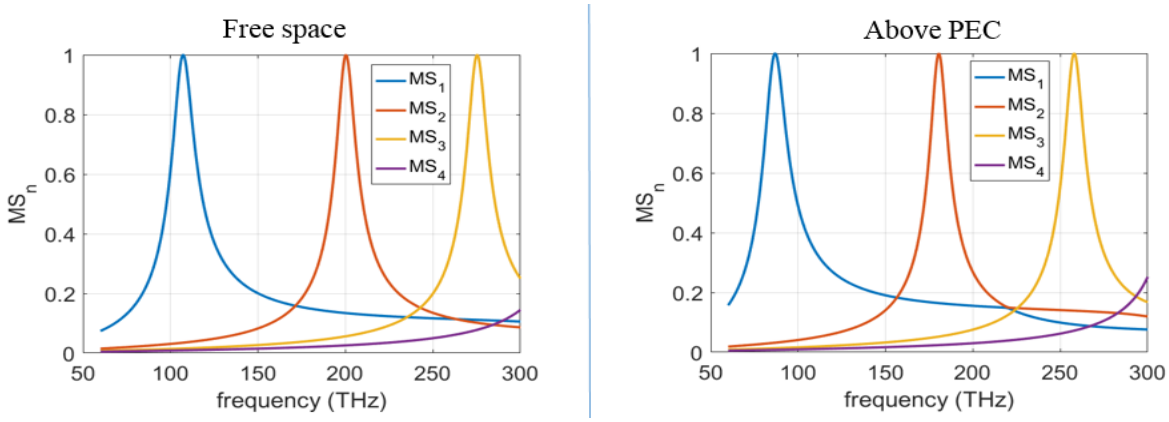

Figure 26 Modal Significance for the first four modes of a gold wire with $L = 600nm$ and $r = 10nm$ suspended in free-space (left), and vertically oriented above a PEC half-space (right).

Significance curves for a gold wire suspended in free-space, and above a PEC half-space. This shows us that besides the characteristic shift in resonant frequency, there does not appear to be any significant change in the relative bandwidth of the resonant peaks, or in the modal overlap.

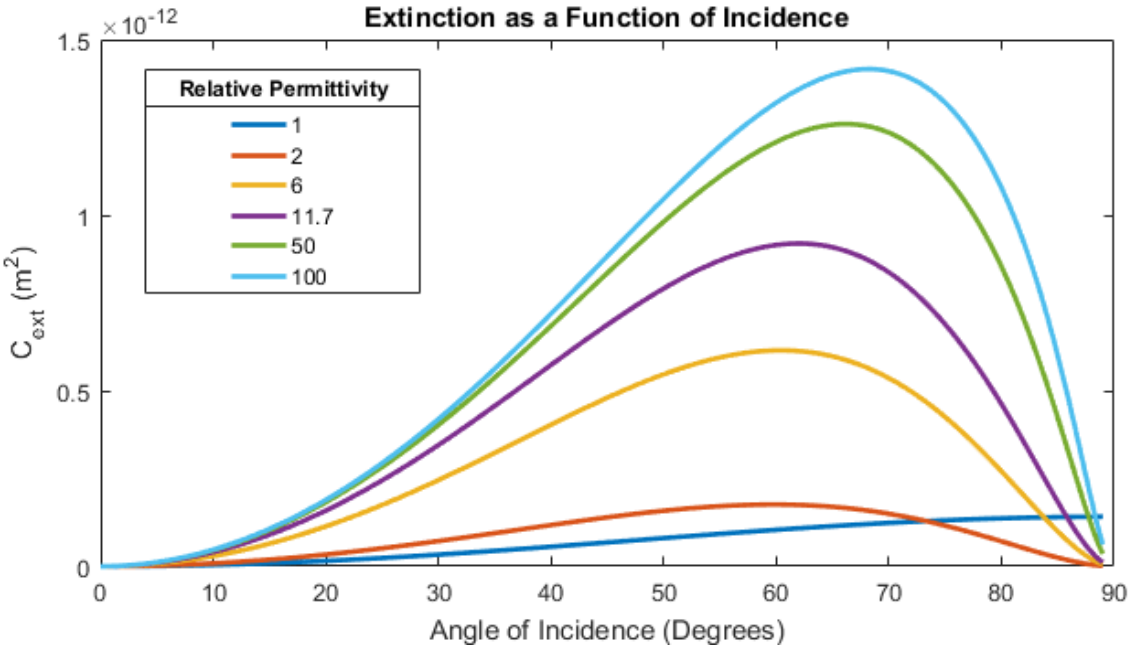

Figure 27 Extinction cross-section as a function of excitation angle of incidence, for a 600nm gold wire above various magnitudes of relative permittivity for the dielectric substrate on which the wire is placed.

As previously noted, the presence of the interface does have some considerable effect on the scattering characteristics and radiation pattern of the wire [7]. For the wire in free-space, we naturally assume that the greatest coupling with the electric field will occur when that field vector is perfectly parallel to the axial component of the wire, or from the diagram in the inset of Figure 25, when the angle of incidence is $\theta_i = 90^o$. From Figure 27, we see that this is indeed the case, for when the relative permittivity of the dielectric substrate is equal to 1, the greatest coupling, and therefore the greatest extinction, occurs when $\theta_i = 90^o$. But as the relative permittivity of the half-space is increased from that of free-space, we see that the maximum coupling no longer occurs when $\theta_i = 90^o$. Rather, we find that the greatest extinction occurs when the angle of incidence is approximately between $60^o < \theta_i <$

70^o. Furthermore, we find that the maximum extinction initially decreases and then increases as permittivity in the half-space increases, with a relative minima at $\varepsilon \approx 1.3$. To explain this, we must consider that the total electric field seen by the wire is a superposition of both the incident field and a reflected field. Because the interface is not perfectly reflective, we must also consider transmission into the medium and any effect on polarization that might occur at the interface. These effects are considered by Fresnel's equations. For the case of an electric field propagating parallel to the plane of incidence, the ratio of the reflected wave to the incident wave is given as,

$$\Gamma_{||} = \frac{E_r}{E_i} = \frac{\eta_2 cos\theta_t - \eta_0 cos\theta_i}{\eta_2 cos\theta_t + \eta_0 cos\theta_i} \tag{31}$$

where $\eta = \sqrt{j\omega\mu/(\sigma + j\omega\varepsilon)}$, and the angle of transmission, θ_t, is given by Snell's law as, $n_1 sin\theta_i = n_2 sin\theta_t$, where $n_1 = c\sqrt{\varepsilon_1}$ and $n_2 = c\sqrt{\varepsilon_2}$ are the refractive indices for the medium above and below the interface, respectively. If we then consider the following equation where the total field seen by the nanowire is expressed in terms of the incident and reflected fields, and the reflected field, E_r, is shown in terms of the incident field, E_r, and the reflection coefficient, $\Gamma_{||}$,

$$\boldsymbol{E}_{tot} = \boldsymbol{E}_i sin\theta_i (1 - \Gamma_{||}) \tag{32}$$

we see that the total field seen by the wire can be expressed as the component of the incident field parallel to the wire with a reflection term. Figure 28 shows $\Gamma_{||}$ with respect to angle of

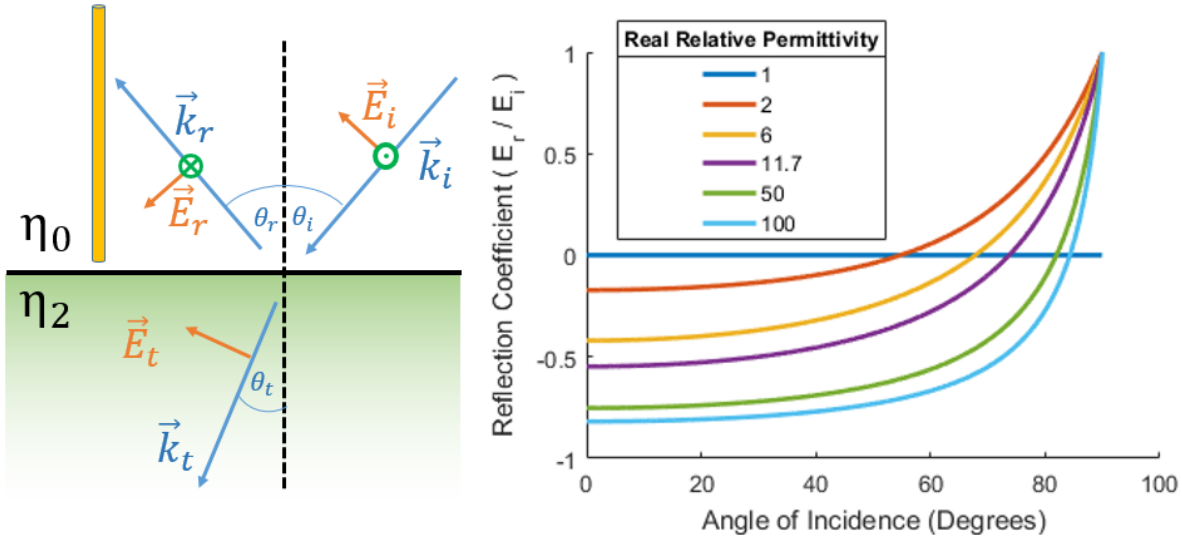

Figure 28 (left) Diagram of a wire in the presence of incident, transmitted, and reflected fields from an interface, and (right) Reflection Coefficient curves

incidence, θ_i, for multiple half-space permittivities. We see that for every relative permittivity, $\varepsilon > 1$, $\Gamma_{||}$ is negative for small angles, but eventually crosses zero to become positive at some particular angle. The angle at which this occurs is known as Brewster's Angle, and represents a change in the polarization of the electric field [36]. The ultimate effect is that as θ_i increases from 0, $\boldsymbol{E}_i sin\theta_i$ also increases. This magnitude is weighted by $1 - \Gamma_{||}$, which is decreasing from 2 to 0 over the domain $0^o < \theta_i < 90^o$. The final result is an extinction pattern similar to what we see in Figure 27.

A characteristic modes approach will show that a change in the impedance of the interface, will result in changes to the coupling of each mode with the incident field. This relationship will ultimately determine the radiation pattern for the wire in each case. If we

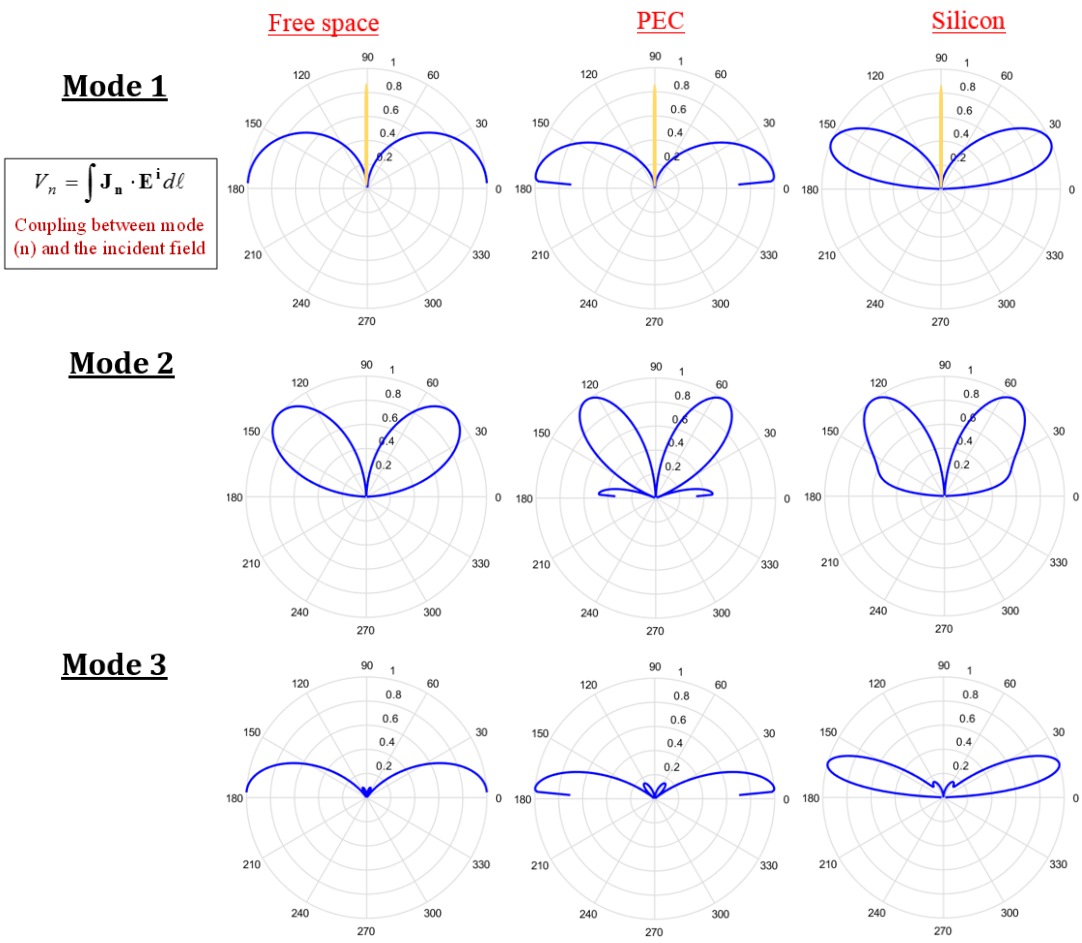

Figure 29 Individually normalized MEC's for the first three modes (from top to bottom) for a gold wire in free-space (left column), above a PEC (middle column), and above silicon (right column).

consider Figure 29, we see that, similarly to Figure 27, there is a significant difference between the MEC pattern for the free-space case and wires above an interface. We see that the presence of an interface will shift the angle of the main lobe of radiation, and for higher modes, will reveal the emergence of side-lobes. More importantly, the presence of the interface creates nulls at angles parallel to the interface for any frequency. Figure 30 shows how the Modal Significance and Modal Excitation Coefficients may be used to determine the total radiation patterns. Consider the frequency point, f_1 on the Modal Significance plot of Figure 30a. We

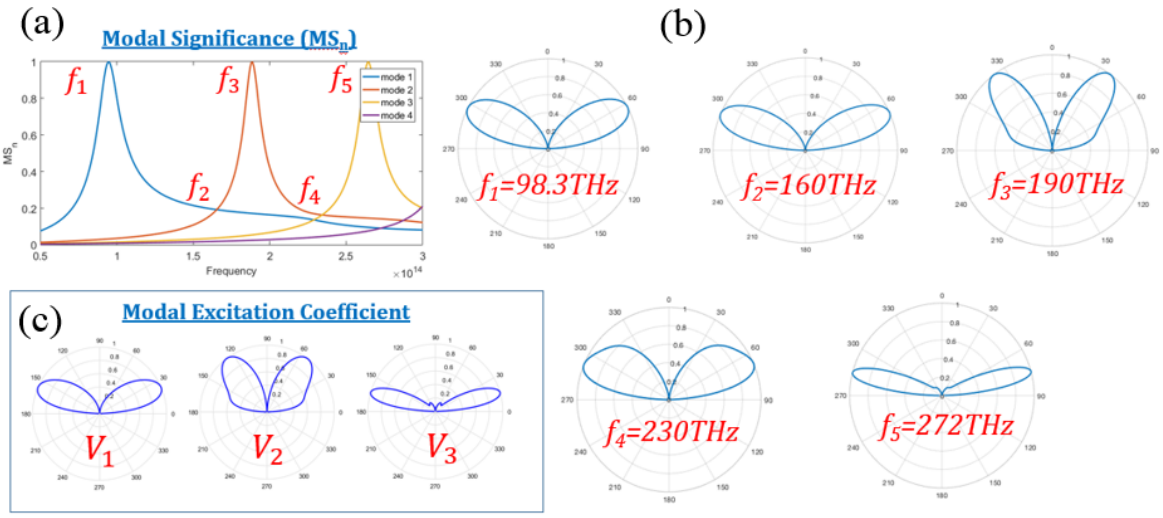

Figure 30 Modal Significance for first 3 modes (a), MEC's (V_n) for first 3 modes (c), and normalized extinction plots, for a 600 nm gold wire above a silicon substrate (b).

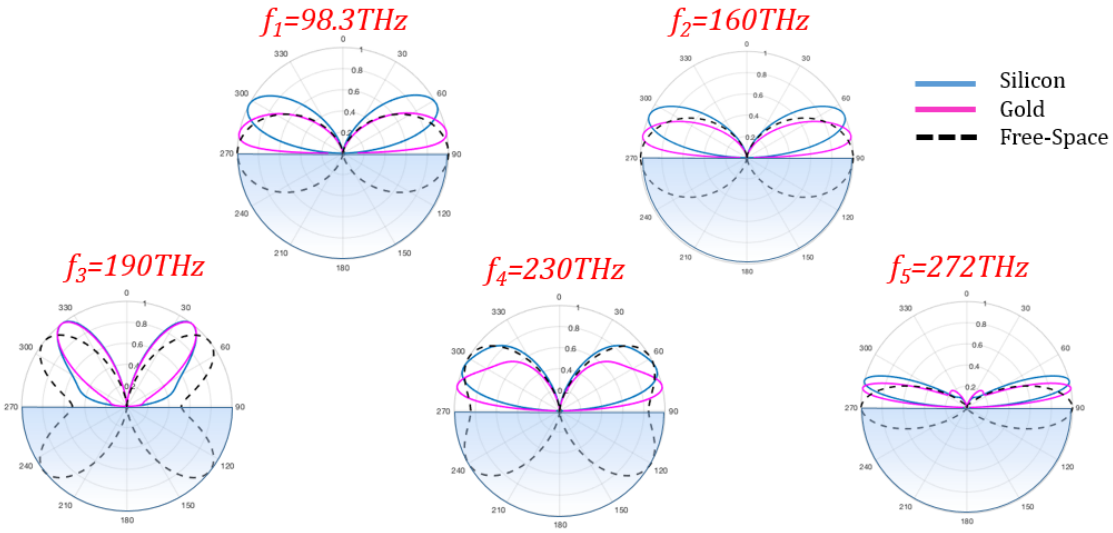

Figure 31 Comparison of normalized extinction cross-section for a 600 nm gold wire above silicon, above gold, and in free-space, at five specific frequencies.

see that at this frequency, Mode 1 is completely dominant, with a negligible contribution from any other modes. We then expect to find that the radiation pattern at this frequency should be nearly identical in form to the Mode 1 MEC, which we see is indeed the case. At f_2 we see that

the contributions from Mode 1 and Mode 2 are equal, so we might expect to find that the radiation pattern at that frequency is an even mixture of the Mode 1 and Mode 2 MEC's. This is, of course, the case. However, because the polar plots in Figure 30c are self-normalized, we do not see that the Mode 2 MEC is much lower in magnitude than the Mode 1 MEC. Therefore, the radiation pattern at f_2 more closely resembles the Mode 1 MEC. At f_3, however, we see that the domination of Mode 2 results in a radiation pattern that very closely resembles the Mode 2 MEC. At f_4 we find an interesting case, in that all of the first three modes share an equal significance resulting in a radiation pattern that reflects a mixture of all three MEC's. For comparison, Figure 31 shows normalized polar plots of the extinction cross-section, for a 600 nm gold wire, in free-space, above silicon, and above a gold interface, at each of the same five frequencies as shown in Figure 30.

Finally, we consider the effect of the permittivity of the lower half-space on radiation below the interface. If we consider the typical case where the refractive index of the upper half-space is less than that of the lower, from Snell's law, $n_1 sin\theta_i = n_2 sin\theta_t$, we find that the angle of transmission will always be less than the angle of reflection, with respect to the interface normal, as is illustrated in Figure 32. In the limiting case of $\theta_i = 90^o, \theta_t$ will be some angle less than 90^o and determined from the relative permittivity of the medium from the relationship, $\sin^{-1}\frac{\sqrt{\varepsilon_1}}{\sqrt{\varepsilon_2}} = \theta_{crit}$, or the critical angle. Subsequently, no radiation should occur beyond this critical angle. Because of this restriction, all radiation is constricted to a particular beam angle, resulting in a lensing effect. We see that this lensing reduces the beam-width, which concentrates the radiated power to a smaller radial area. This leads to a large gain in the power of the main lobes in the dielectric with respect to the main lobes above the interface, which can be seen from the plots in Figure 33. If we consider the 600 nm gold wire above an

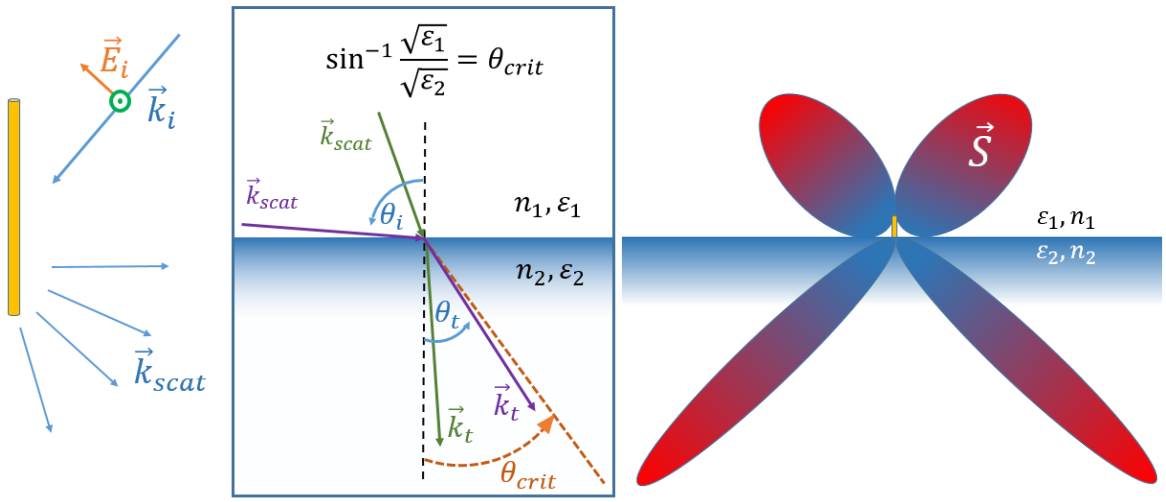

Figure 32 Diagram of dielectric lensing of scattered fields.

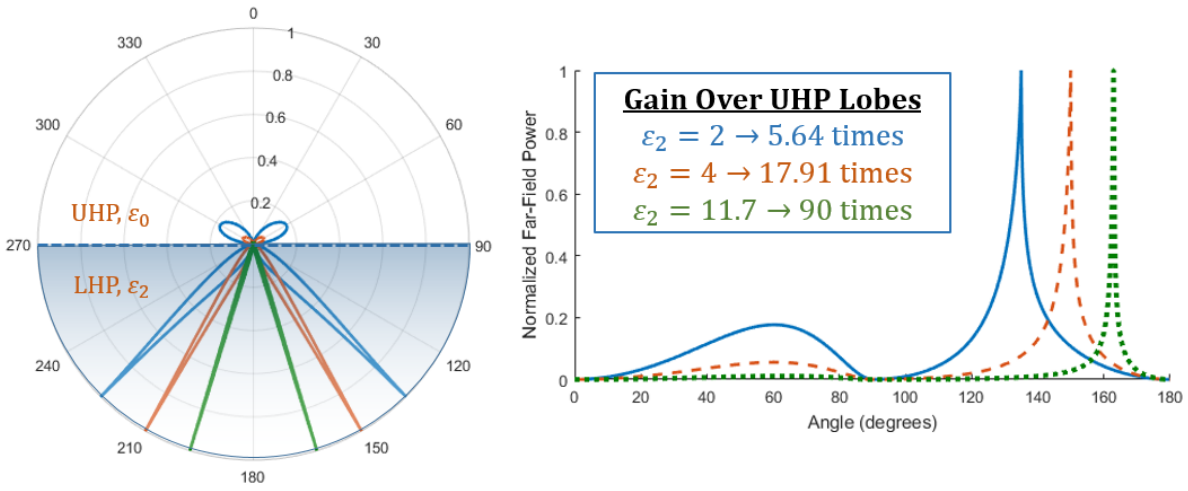

Figure 33 Comparison of far-field radiation patterns for a 600 nm gold wire above an interface with varying relative permittivity.

interface at the wire's first resonant frequency $f_0 \approx 100\,THz$, we see that the power radiated in the far-field is concentrated to a smaller beam-width below the interface compared to the main lobes of the upper half-space. Furthermore, we see that the main beam angle corresponds closely with the critical angle relative to that permittivity. In the case of the gold wire above a

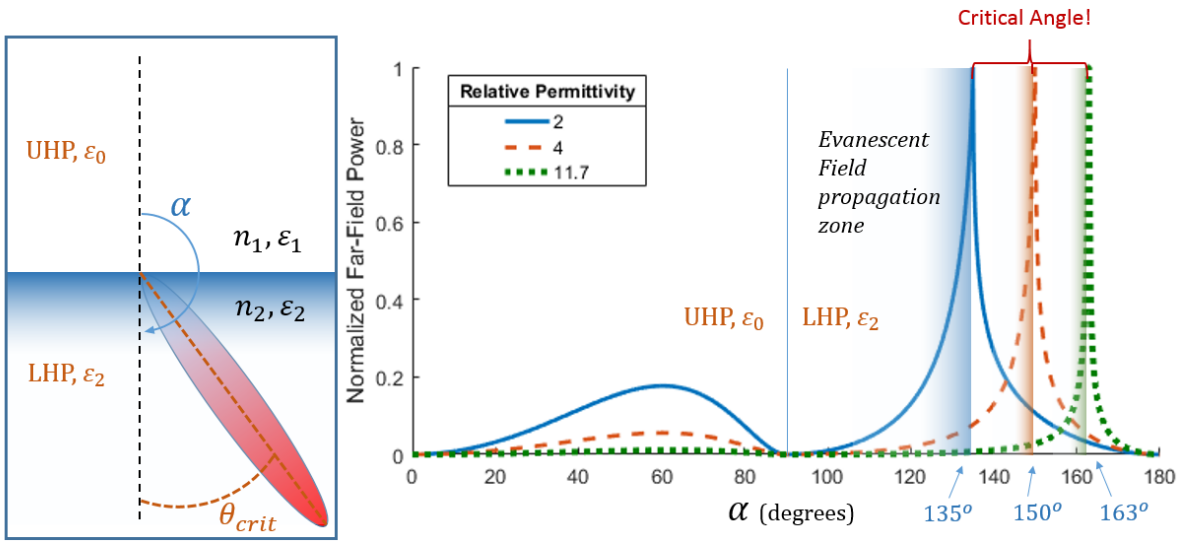

Figure 34 Comparison of far-field radiation patterns for a 600 nm gold wire above an interface with varying relative permittivity, showing radiation beyond critical angle.

silicon substrate, we find approximately 90 times more power radiated into the substrate then into the air above, as seen in Figure 33. Curiously, we also find that a considerable amount of power is being radiated just beyond the critical angle, as can be seen in the right plot of Figure 34. This phenomenon is explained by Lukosz and Kuntz [25] as evanescent fields that couple with the dielectric and contribute to the overall radiated power when the height of the wire above the interface is less than the emission wavelength. The contribution of these evanescent waves decays rapidly as the distance of the dipole from the interface becomes $h \geq \lambda$, as can be seen by Figure 35. We see that as the contribution of the evanescent waves decreases, radiation past the critical angle also decreases. Furthermore, Lukosz and Kunz conclude that, in general, an electric or magnetic dipole in very close proximity to the boundary of a medium with $n_2 > n_1$ will radiate predominantly into the denser medium regardless of in which medium the dipole actually lies. This assessment agrees with the results in Figures 33-35.

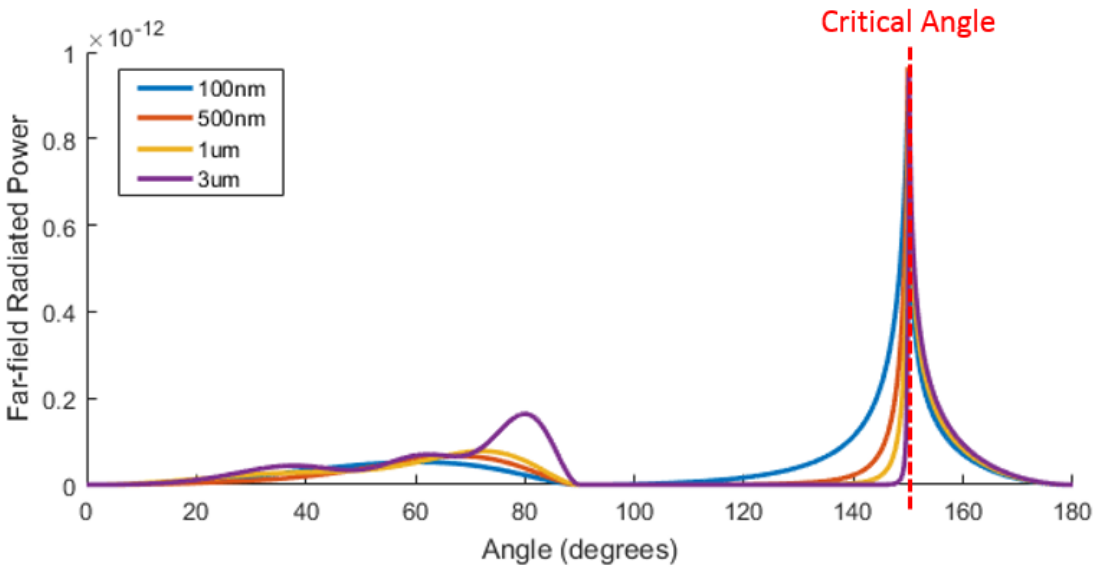

Figure 35 Far-field radiation for 600nm gold wire above a substrate with $\varepsilon_2 = 4$, with varying height above interface.

5.5 Effect of Multiple Vertical Wires

When we take the previous case of the vertical wire and expand it to include multiple wires, such as in a CNT forest, we find that we must also consider the mutual coupling of the wires due to their proximity. Our initial investigation into this case reveal some interesting results. We find from the results in Figure 36, that first and foremost, our implementation of the MOM for ATW formulation is accurate for the case of multiple wires, when compared with 3D full-wave simulation in FEKO. Next, we find that the proximity of the wires to each other affects their resonant frequency, when compared to the case of a single wire. For the single, 600 nm, gold wire in free-space, we expect a resonant frequency at approximately 110 THz. When the same wire is located 1 nm above a silicon substrate, we find that the frequency is shifted down to about 91 THz. However, for the case of three wires of the same length $L =$

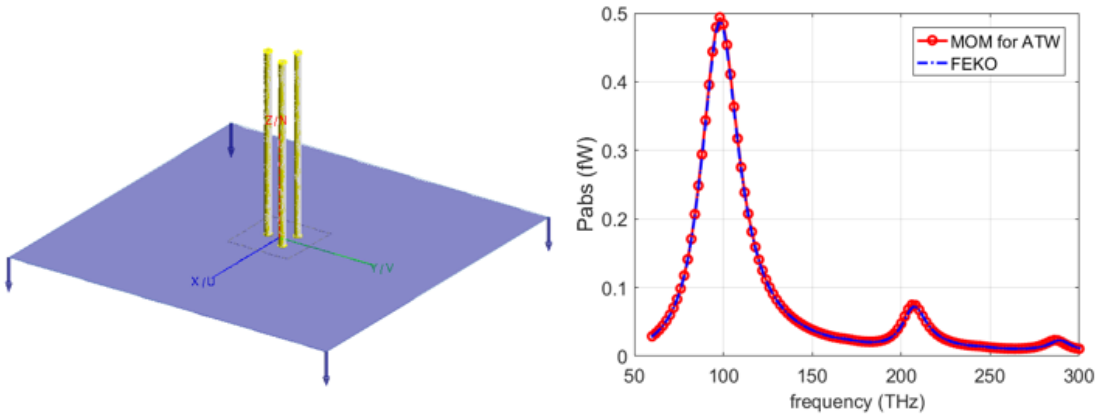

Figure 36 (left) 3D model of FEKO simulation of three 600 nm gold wires with a 10 nm radius vertically oriented at 1 nm above silicon. (right) Comparison of FEKO simulation with MOM for ATW formulation.

$600\ nm$ located 1 nm above silicon, we find that the resonant frequency is shifted back up closer to 100 THz. This shows that the effect of their mutual coupling is strong enough to balance the effect of the substrate.

If we then consider the case where two wires of length $L = 600\ nm$ are located at $h = 1\ nm,$ and $h = 20\ nm,$ respectively, as in Figure 37, we see that, when these two wires are suspended in free-space the 19 nm difference in height has a negligible effect compared to the effect of mutual coupling on the resonance. When the presence of a silicon interface is included, however, we find there is a split in the resonance. This is because the effect of the interface on resonance of the wire at a 20 nm height is negligible compared to the wire at a height of 1 nm, as we recall from Figure 25. For this reason, the two resonances begin to differentiate from each other with a change in height from the substrate. This effect might also be accomplished with wires of various lengths, although these simulations have yet to be performed. A more exhaustive analysis on the effect of multiple wires is certainly intended for future work, with the results of this section being only a preliminary analysis.

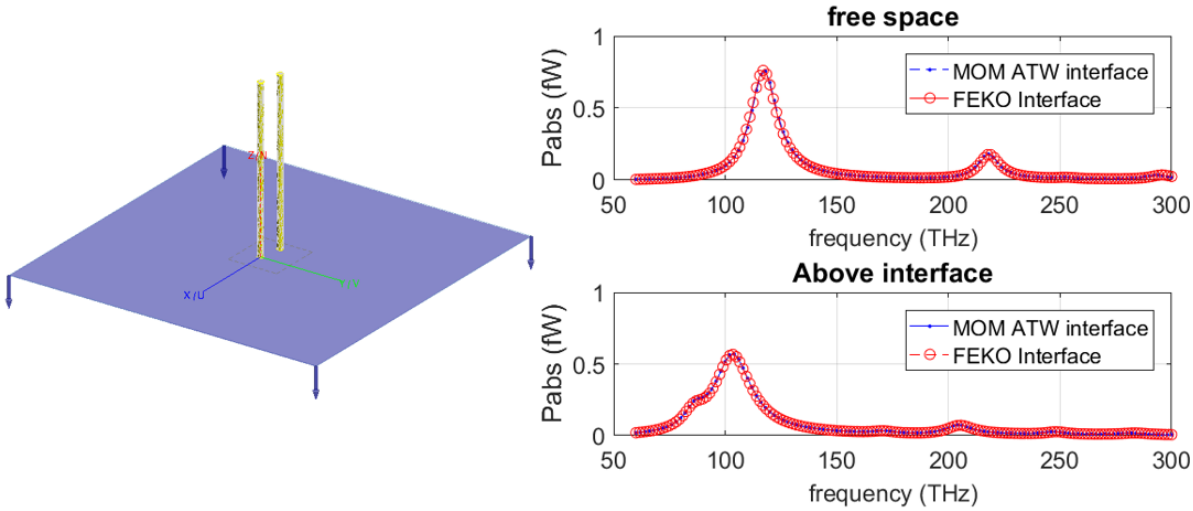

Figure 37 (left) 3D model of FEKO simulation of two 600 nm gold wires with a 10 nm radius vertically oriented at 1 nm and 20 nm above silicon. Both wires are separated by a distance of 64 nm. (right) Comparison of FEKO simulation with MOM for ATW formulation.

CHAPTER 6

CONCLUSION AND FUTURE DIRECTION

In this thesis, a Theory of Characteristic Modes approach was taken to predict the current distributions, scattering, and absorption of nano-wires and micro-wires, composed of various materials, in the presence of a lossy dielectric half-space. This was accomplished initially, through the implementation of an arbitrarily thin wire approximation for the Method of Moments formulation, along with a modified Green's function to account for the interface. The result of this particular implementation was a quite significant reduction in computational time and/or resources necessary to complete the computational analysis of wires with large aspect ratios above an infinite half-space. Next, the Theory of Characteristic Modes was augmented to consider non-perfectly conducting wires so that wires composed of various materials, such as metals, carbon nanotubes and magnetic materials, could be analyzed. The results of this analysis showed that the material impedance has a significant effect on resonant frequency, resonant bandwidth, and modal overlap or current distribution.

After characterization of the individual wire, the effects of the presence of a lossy dielectric half-space were considered. This analysis showed that the impedance of the substrate also has a significant effect on the resonant frequency of the wire, however the impact on bandwidth of the wire resonance is negligible. Furthermore, it was shown that the impedance of the interface also results in significant changes to the radiation pattern of the wire, when compared to that of the wire in free-space. We found that wires in close proximity to the interface between air and a dielectric will radiate most of its power into the substrate, with highly directional beams caused by dielectric lensing. These results were further clarified by a Characteristic Mode Analysis which showed methods for mixing modes to obtain desired

radiation patterns. Finally, an introduction into an analysis of multiple wires was given, suggesting that the proximity of individual wires to one another, as well as relative height above the dielectric, has a strong impact on resonant frequency and may very well be modified to produce a broadband response.

In general, the wire material and geometry, proximity to other wires and interfaces, as well as the properties of the interface itself, may all be used as tuning mechanisms. Furthermore, this work suggests that, although special care is needed when considering nanoscale structures at near-infrared and optical frequencies, CMA is a robust and powerful tool for optimizing nanowire structures for a particular solution.

The future direction of this work is to complete a more comprehensive analysis on the interactions of multiple vertical wires above a substrate, while simultaneously implementing Green's function modifications that consider arbitrarily oriented wires above and inside a lossy dielectric. Near-field simulations considering the field enhancements in the substrate due to the dielectric effects should also be completed. Ultimately, the final goal of this research is to predict the scattering and absorption characteristics of multiple wires of arbitrary shape, embedded above or inside a dielectric multilayer structure.

LIST OF REFERENCES

1. Alber, I., Sigle, W., Müller, S., Neumann, R., Picht, O., Rauber, M., ... & Toimil-Molares, M. E. (2011). Visualization of multipolar longitudinal and transversal surface plasmon modes in nanowire dimers. *ACS nano*, *5*(12), 9845-9853.
2. Blaber, M. G., Arnold, M. D., & Ford, M. J. (2009). Search for the ideal plasmonic nanoshell: the effects of surface scattering and alternatives to gold and silver. *The Journal of Physical Chemistry C*, *113*(8), 3041-3045.
3. Cabedo-Fabres, M., Antonino-Daviu, E., Valero-Nogueira, A., & Bataller, M. F. (2007). The theory of characteristic modes revisited: A contribution to the design of antennas for modern applications. *IEEE Antennas and Propagation Magazine*, *49*(5), 52-68.
4. Capek, M., Hamouz, P., Hazdra, P., & Eichler, J. (2013). Implementation of the Theory of Characteristic Modes in MATLAB. *IEEE Antennas and Propagation Magazine*, *55*(2), 176-189.
5. Chen, Y., & Wang, C. F. (2014, July). Surface integral equation based characteristic mode formulation for dielectric resonators. In *Antennas and Propagation Society International Symposium (APSURSI), 2014 IEEE* (pp. 846-847). IEEE.
6. Durbhakula K., Hassan A. M., Vargas-Lara F., Chatterjee D., Gaffar M., Douglas J. F., and Garboczi E. J. (2017). Electromagnetic Scattering from Individual Crumpled Graphene Flakes: A Characteristic Modes Approach. *IEEE Trans. on Antennas and Propagation (In Review)*.

7. Engheta, N., Papas, C. H., & Elachi, C. (1982). Radiation patterns of interfacial dipole antennas. *Radio Science*, *17*(6), 1557-1566.
8. Fabres, M. C. (2007). Systematic design of antennas using the theory of characteristic modes. *Columbus*.
9. Garbacz, R. J. (1965). Modal expansions for resonance scattering phenomena. *Proceedings of the IEEE*, *53*(8), 856-864.
10. Gibson, W. C. (2014). *The method of moments in electromagnetics*. CRC press.
11. Guan, L., Ding, D., Fan, Z., Li, M., Li, Z., & Chen, R. (2016, March). Analysis of dielectric resonator antennas using characteristic modes. In *Wireless Information Technology and Systems (ICWITS) and Applied Computational Electromagnetics (ACES), 2016 IEEE/ACES International Conference on* (pp. 1-2). IEEE.
12. Hanson, G. W. (2005). Fundamental transmitting properties of carbon nanotube antennas. *IEEE Transactions on antennas and propagation*, *53*(11), 3426-3435.
13. Hao, J., & Hanson, G. W. (2006). Electromagnetic scattering from finite-length metallic carbon nanotubes in the lower IR bands. *Physical Review B*, *74*(3), 035119.
14. Harrington, R., Mautz, J., & Chang, Y. (1972). Characteristic modes for dielectric and magnetic bodies. *IEEE-44 Transactions on Antennas and Propagation*, *20*(2), 194-198.
15. Harrington, R., & Mautz, J. (1971). Computation of characteristic modes for

conducting bodies. *IEEE Transactions on Antennas and Propagation*, *19*(5), 629-639.

16. Harrington, R., & Mautz, J. (1971). Theory of characteristic modes for conducting bodies. *IEEE Transactions on Antennas and Propagation*, *19*(5), 622-628.

17. Hassan, A. M., Vargas-Lara, F., Douglas, J. F., & Garboczi, E. J. (2016). Electromagnetic resonances of individual single-walled carbon nanotubes with realistic shapes: A characteristic modes approach. *IEEE Transactions on Antennas and Propagation*, *64*(7), 2743-2757.

18. Hernando, A., Lopez-Dominguez, V., Ricciardi, E., Osiak, K., & Marin, P. (2016). Tuned scattering of electromagnetic waves by a finite length ferromagnetic microwire. *IEEE Transactions on Antennas and Propagation*, *64*(3), 1112-1115.

19. Johnson, P. B., & Christy, R. W. (1972). Optical constants of the noble metals. *Physical review B*, *6*(12), 4370.

20. Kharisov, B. I., Kharissova, O. V., García, B. O., Méndez, Y. P., & de la Fuente, I. G. (2015). State of the art of nanoforest structures and their applications. *RSC Advances*, *5*(128), 105507-105523.

21. Kremers, C., & Chigrin, D. N. (2011). Light scattering on nanowire antennas: A \ semi-analytical approach. *Photonics and Nanostructures-Fundamentals and Applications*, *9*(4), 358-366.

22. Lepro, X., Lima, M. D., & Baughman, R. H. (2010). Spinnable carbon nanotube forests grown on thin, flexible metallic substrates. *Carbon*, *48*(12), 3621-3627.

23. Liberal, I., Ederra, I., Gomez-Polo, C., Labrador, A., Perez-Landazabal, J. I., & Gonzalo, R. (2012). A comprehensive analysis of the absorption spectrum of conducting ferromagnetic wires. *IEEE Transactions on Microwave Theory and Techniques*, *60*(7), 2055-2065.

24. Lukosz, W., & Kunz, R. E. (1977). Light emission by magnetic and electric dipoles close to a plane interface. I. Total radiated power. *JOSA*, *67*(12), 1607-1615.

25. Lukosz, W., & Kunz, R. E. (1977). Light emission by magnetic and electric dipoles close to a plane dielectric interface. II. Radiation patterns of perpendicular oriented dipoles. *JOSA*, *67*(12), 1615-1619.

26. Miers, Z. T., & Lau, B. K. (2016). Computational analysis and verifications of characteristic modes in real materials. *IEEE Transactions on Antennas and Propagation*, *64*(7), 2595-2607.

27. Miller, E. K., Poggio, A. J., Burke, G. J., & Selden, E. S. (1972). Analysis of wire antennas in the presence of a conducting half-space. Part I. The vertical antenna in free space. *Canadian Journal of Physics*, *50*(9), 879-888.

28. Miller, E. K., Poggio, A. J., Burke, G. J., & Selden, E. S. (1972). Analysis of wire antennas in the presence of a conducting half-space. Part II. The horizontal antenna in free space. *Canadian Journal of Physics*, *50*(21), 2614-2627.

29. Mittra, R., Parhami, P., & Rahmat-Samii, Y. (1979). Solving the current element problem over lossy half-space without Sommerfeld integrals. *IEEE Transactions on Antennas and Propagation*, *27*(6), 778-782.

30. Myroshnychenko, V., Rodríguez-Fernández, J., Pastoriza-Santos, I., Funston, A. M.,

Novo, C., Mulvaney, P., ... & de Abajo, F. J. G. (2008). Modelling the optical response of gold nanoparticles. *Chemical Society Reviews*, *37*(9), 1792-1805.

31. Novotny, L. (2007). Effective wavelength scaling for optical antennas. *Physical Review Letters*, *98*(26), 266802.

32. Ordal, M. A., Long, L. L., Bell, R. J., Bell, S. E., Bell, R. R., Alexander, R. W., & Ward, (1983). Optical properties of the metals al, co, cu, au, fe, pb, ni, pd, pt, ag, ti, and w in the infrared and far infrared. *Applied Optics*, *22*(7), 1099-1119.

33. Parhami, P., Rahmat-Samii, Y., & Mittra, R. (1980). An efficient approach for evaluating Sommerfeld integrals encountered in the problem of a current element radiating over lossy ground. *IEEE Transactions on Antennas and Propagation*, *28*(1), 100-104.

34. Rahmat-Samii, Y., Parhami, P., & Mittra, R. (1978). Loaded horizontal antenna over an imperfect ground. *IEEE Transactions on Antennas and Propagation*, *26*(6), 789-796.

35. Raines, B. D., & Rojas, R. G. (2012). Wideband characteristic mode tracking. *IEEE Transactions on Antennas and Propagation*, *60*(7), 3537-3541.

36. Sadiku, M. N. (2014). *Elements of electromagnetics*. Oxford university press.

37. Sarkar, T. K. (1977). Analysis of arbitrarily oriented thin wire antennas over a plane imperfect ground. *Archiv Elektronik und Uebertragungstechnik*, *31*, 449-457.

38. Shampine, L. F. (2008). Vectorized adaptive quadrature in MATLAB. *Journal of Computational and Applied Mathematics*, *211*(2), 131-140.

39. Smith, N. V. (1969). Optical constants of sodium and potassium from 0.5 to 4.0 eV

by split-beam ellipsometry. *Physical Review*, *183*(3), 634.

40. Sommerfeld, A. (1949). *Partial differential equations in physics* (Vol. 1). Academic press.

41. Volakis, J. L., Sertel, K. (2012). *Integral Equation Methods for Electromagnetics*. Scitech Publishing.

42. Willis, K. J., Hagness, S. C., & Knezevic, I. (2013). A generalized Drude model for doped silicon at terahertz frequencies derived from microscopic transport simulation. *Applied Physics Letters, 102*(12), 122113.

43. Wu, Q., & Su, D. (2013). A broadband model of the characteristic currents for rectangular plates. *IEEE Transactions on Electromagnetic Compatibility*, *55*(4), 725-732.

44. Xu, X. B., & Huang, Y. (2007). An efficient analysis of vertical dipole antennas above a lossy half-space. *Progress In Electromagnetics Research*, *74*, 353-377.

45. Ylä-Oijala, P., Tzarouchis, D. C., Raninen, E., & Sihvola, A. (2017). Characteristic mode analysis of plasmonic nanoantennas. *IEEE Transactions on Antennas and Propagation*, *65*(5), 2165-2172.

VITA

Daniel Scott Kiddle was born on November 16, 1983, in Iowa City, IA. After serving in the United States Navy as an Electronic Warfare Technician, he was honorably discharged and went on to pursue a career in music production, earning a certification in audio engineering from the Institute for Audio Engineering Arts, in Kansas City, MO in 2009. After several years pursuing music, he returned to academia where he graduated Magna Cum Laude with his Bachelors of Science in Electrical and Computer Engineering from the University of Missouri-Kansas City in 2016. After receiving his Bachelor's degree, he continued in the Master of Science program in Electrical Engineering at the University of Missouri-Kansas City while working full-time as an Electrical Engineer at the National Security Campus managed by Honeywell. Mr. Kiddle is a member of the Tau Beta Pi, and Etta Kappa Nu honor societies, as well as the IEEE.